Cell Reports

Article

Circadian Modulation of Neurons and Astrocytes Controls Synaptic Plasticity in Hippocampal Area CA1

Graphical Abstract

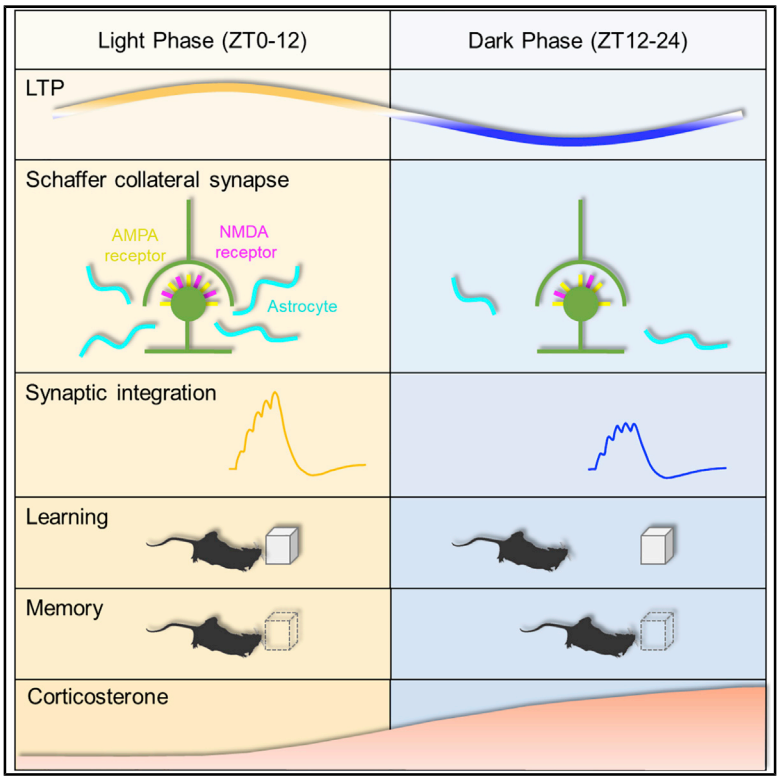

Highlights

- Hippocampal plasticity varies with circadian rhythmicity
- Neurons reduce the surface expression of NMDA receptors during the dark phase
- Astrocytes retract their processes from synapses during the dark phase
- These effects alter synaptic integration and hippocampal-dependent learning

Authors

John P. McCauley, Maurice A. Petroccione, Lianna Y. D'Brant, ..., Damian G. Zuloaga, Michele Migliore, Annalisa Scimemi

Correspondence

scimemia@gmail.com, ascimemi@albany.edu

In Brief

McCauley et al. shed light on the molecular and cellular mechanisms that allow hippocampal neurons and astrocytes to shape circadian changes in synaptic plasticity and hippocampal-dependent behaviors. They identify corticosterone as a key molecule mediating these effects, capable of tuning the temporal dynamics of cognitive processing in mice.

McCauley et al., 2020, Cell Reports *33*, 108255
October 13, 2020
https://doi.org/10.1016/j.celrep.2020.108255

CellPress

Cell Reports

CellPress
OPEN ACCESS

Article

Circadian Modulation of Neurons and Astrocytes Controls Synaptic Plasticity in Hippocampal Area CA1

John P. McCauley,[1,11] Maurice A. Petroccione,[1,11] Lianna Y. D'Brant,[1,2] Gabrielle C. Todd,[1] Nurat Affinnih,[1] Justin J. Wisnoski,[1] Shergil Zahid,[1] Swasti Shree,[1,3] Alioscka A. Sousa,[4,5] Rose M. De Guzman,[6] Rosanna Migliore,[7] Alexey Brazhe,[8,9] Richard D. Leapman,[5] Alexander Khmaladze,[2] Alexey Semyanov,[9,10] Damian G. Zuloaga,[6] Michele Migliore,[7] and Annalisa Scimemi[1,12,*]

[1]Department of Biology, SUNY Albany, 1400 Washington Avenue, Albany, NY 12222, USA
[2]Department of Physics, SUNY Albany, 1400 Washington Avenue, Albany, NY 12222, USA
[3]Bethlehem Central High School, 700 Delaware Avenue, Delmar, NY 12054, USA
[4]Federal University of São Paulo, Department of Biochemistry, 100 Rua Tres de Maio, São Paulo 04044-020, Brazil
[5]National Institute of Biomedical Imaging and Bioengineering, National Institutes of Health, 9000 Rockville Pike, Bethesda, MD 20892, USA
[6]Department of Psychology, SUNY Albany, 1400 Washington Avenue, Albany, NY 12222, USA
[7]Institute of Biophysics, National Research Council, 153 Via Ugo La Malfa, Palermo 90146, Italy
[8]Department of Biophysics, Lomonosov Moscow State University, Leninskie Gory 1/12, Moscow 119234, Russia
[9]Department of Molecular Neurobiology, Institute of Bioorganic Chemistry, Ulitsa Miklukho-Maklaya 16/10, Moscow 117997, Russia
[10]Sechenov First Moscow State Medical University, Bolshaya Pirogovskaya Ulitsa 19c1, Moscow 119146, Russia
[11]These authors contributed equally
[12]Lead Contact
*Correspondence: scimemia@gmail.com or ascimemi@albany.edu
https://doi.org/10.1016/j.celrep.2020.108255

SUMMARY

Most animal species operate according to a 24-h period set by the suprachiasmatic nucleus (SCN) of the hypothalamus. The rhythmic activity of the SCN modulates hippocampal-dependent memory, but the molecular and cellular mechanisms that account for this effect remain largely unknown. Here, we identify cell-type-specific structural and functional changes that occur with circadian rhythmicity in neurons and astrocytes in hippocampal area CA1. Pyramidal neurons change the surface expression of NMDA receptors. Astrocytes change their proximity to synapses. Together, these phenomena alter glutamate clearance, receptor activation, and integration of temporally clustered excitatory synaptic inputs, ultimately shaping hippocampal-dependent learning *in vivo*. We identify corticosterone as a key contributor to changes in synaptic strength. These findings highlight important mechanisms through which neurons and astrocytes modify the molecular composition and structure of the synaptic environment, contribute to the local storage of information in the hippocampus, and alter the temporal dynamics of cognitive processing.

INTRODUCTION

The circadian rhythmicity with which mammals sleep, feed, regulate their body temperature, and engage in reproductive behaviors is controlled by the main circadian master clock, the suprachiasmatic nucleus (SCN), and the coordinated activity of other semi-autonomous ancillary oscillators in the brain and in peripheral tissues (Guilding and Piggins, 2007). The core molecular transcriptional and translational feedback loops that drive circadian rhythmicity in the SCN are fully established during embryonic development (Namihira et al., 1999; Reick et al., 2001; Sumova et al., 2012; Wakamatsu et al., 2001). Their rhythmic activity is entrained by environmental cues, or zeitgebers, the most potent of which is light (L). The SCN coordinates the activity of subordinate circadian oscillators through neuronal projections confined within the medial hypothalamus, which control corticosteroid release into the bloodstream. Other projections reach the inter-geniculate leaflet and paraventricular nucleus of the thalamus and control melatonin production by the pineal gland (Kalsbeek and Buijs, 2002; Lehman et al., 1987; Meyer-Bernstein et al., 1999; Moore, 1996). In nocturnal animals, corticosteroids and melatonin production peaks in the dark (D; zeitgeber time [ZT] 12–24), with important regulatory effects mediated by receptors expressed broadly throughout the brain and in peripheral organs (Dubocovich et al., 2003; Ishida et al., 2005; Meijer et al., 1998; Moore and Lenn, 1972; Stephan and Zucker, 1972).

The hippocampus is a subordinate circadian oscillator. Here, more than 10% of genes and proteins show circadian fluctuations and are associated with changes in synaptic excitability (Barnes et al., 1977; Debski et al., 2017). Learning and memory formation, two functions that are conserved across species and that in mammals rely on hippocampal activity, are also

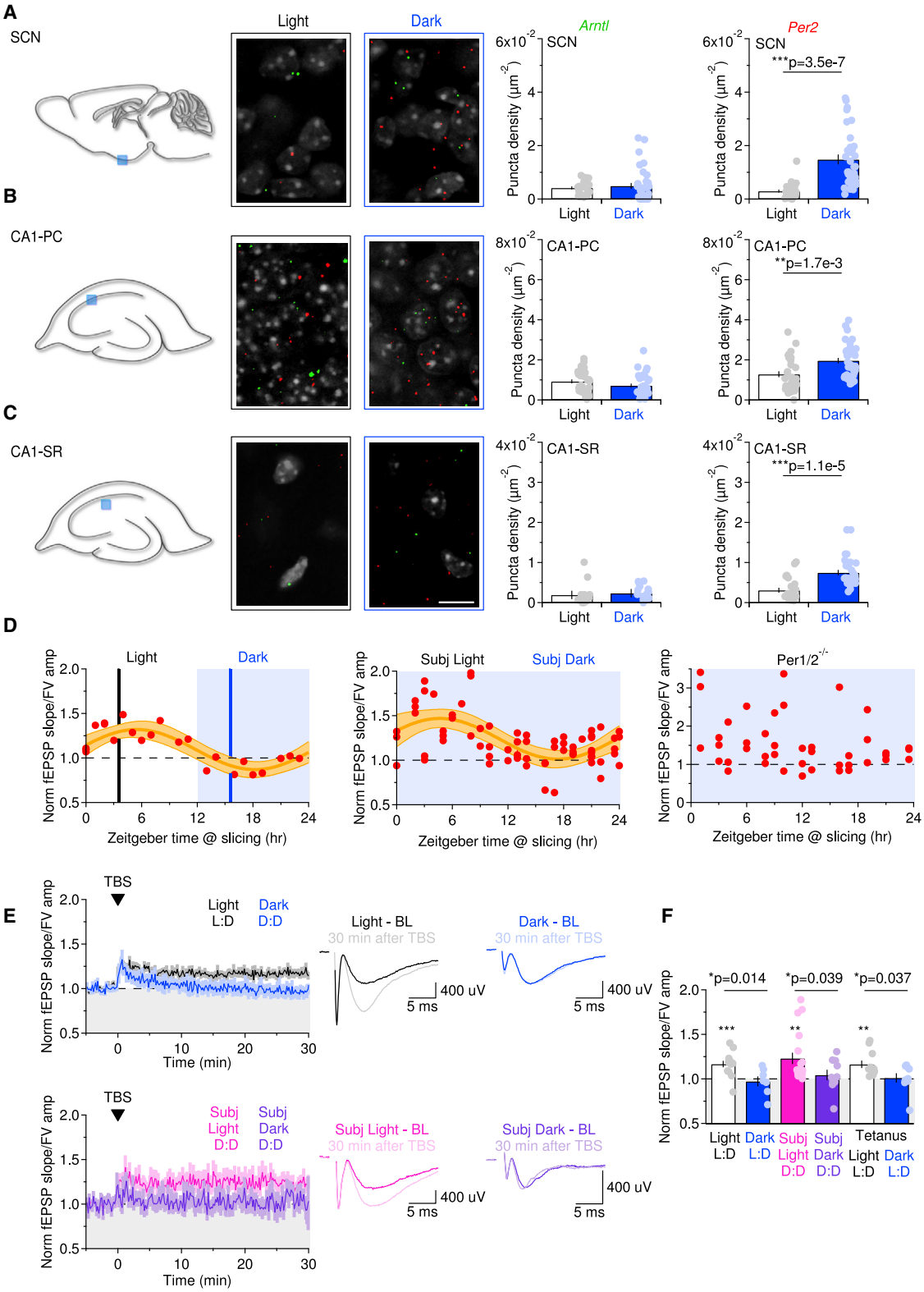

Figure 1. Circadian Changes in Clock Gene Expression and LTP in the Juvenile Mouse Hippocampus

(A) Section structure highlighting the SCN. RNAscope fluorescence *in situ* hybridization (FISH) for *Arntl* (green) and *Per2* (red) in the L/D phases in mice kept under 12 h:12 h L/D conditions (L, n = 28; D, n = 33). Data represent mean ± SEM.

(legend continued on next page)

modulated by circadian rhythms (Gerstner et al., 2009; Rawashdeh et al., 2018; Ruby et al., 2008; Shimizu et al., 2016; Smarr et al., 2014; Snider et al., 2016). Accordingly, mice trained to context fear conditioning protocols acquire the conditioning more slowly if trained in the D phase, a time when long-term plasticity at Schaffer collateral synapses is also reduced (Chaudhury and Colwell, 2002; Winson and Abzug, 1977, 1978). Interestingly, this circadian control of hippocampal function and plasticity is retained in reduced slice preparations, where long-term potentiation (LTP) at hippocampal Schaffer collateral synapses is reduced in slices prepared in the D phase (Harris and Teyler, 1983; Raghavan et al., 1999). The persistence of these effects in slices raise the possibility that they are independent of the ongoing activity of extra-hippocampal inputs and might be due to the presence of one or more diffusible factors that are not easily washed out of slices but whose identity remains enigmatic. Some studies show that increased glucocorticoid levels in the active phase of the circadian cycle facilitate memory formation and cognition (Hui et al., 2004; Whitehead et al., 2013; Yuen et al., 2011). However, other studies suggest that melatonin is both necessary and sufficient for poor memory formation and plasticity in the D phase (Ozcan et al., 2006; Rawashdeh et al., 2007). Glucocorticoid receptors are expressed at different levels throughout the mouse brain, with the exception of the SCN (Balsalobre et al., 2000; Rosenfeld et al., 1988). The expression of mineralocorticoid receptors is more restricted but is abundant in the hippocampus, where melatonin receptors are also present (McEown and Treit, 2011; Musshoff et al., 2002; Qi et al., 2013; Venkova et al., 2009). Here, we ask what accounts for time-of-day changes in LTP at Schaffer collateral synapses and how neurons, astrocytes, and corticosterone contribute to this effect.

RESULTS

The Hippocampus Is a Competent Circadian Oscillator

Central and peripheral circadian clocks are genetically equipped to generate rhythms during embryonic development but continue their maturation in the first postnatal week. At postnatal day 10 (P10), when synaptogenesis in the SCN and other peripheral oscillators is complete, rats show circadian changes in their body temperature (Sumová et al., 2008; Weinert, 2005). We confirmed that this holds true in juvenile mice aged P14–P21 kept under 12 h:12 h L/D (Figure S1A). Their mean body temperature (~35.8°C) displayed consistent oscillations of ±0.5°C every 24.3 ± 5.1 h, with detectable peaks at the end of the L phase and troughs at the end of the D phase. This trend was also present in mice maintained in constant darkness for at least three cycles (12 h:12 h D/D in red dim illumination; Figure S1B). In these mice, the expression of the clock genes *Arntl* and *Per2* was not limited to the SCN and also occurred in the hippocampal CA1 region (Figures 1A–1C). *Per2* expression increased significantly in sections prepared at ZT15.5 (D phase) compared to those prepared at ZT3.5 (L phase) in the SCN, CA1 pyramidal cell (CA1-PC) layer and *stratum radiatum* (*s.r.*). By contrast, the expression of *Arntl* did not change significantly between these two time points in any of these brain regions. Similar results were obtained in mice kept in constant darkness (Figures S1C and S1D). These results are consistent with previous studies in the hippocampus of 4- to 6-month-old mice and in hippocampal slice cultures and expand them, showing that the transcription-translation feedback loops responsible for the circadian regulation of clock gene expression are functional also in the hippocampus of juvenile mice (Kwapis et al., 2018; Namihira et al., 1999; Wang et al., 2009).

Circadian Rhythmicity Shapes Long-Term Plasticity at Schaffer Collateral Synapses

Previous studies showed that the magnitude and incidence of LTP at Schaffer collateral synapses in acute hippocampal slices varies between the L and D phase, but the exact time course of this effect was not determined (Harris and Teyler, 1983; Raghavan et al., 1999). To do this, we induced LTP using a theta burst stimulation (TBS) protocol that mimics the endogenous electroencephalographic activity of the rodent hippocampus during exploratory learning tasks (Buzsáki, 2002) in slices prepared at different ZTs (Figure 1D, left). The magnitude of LTP changed with circadian rhythmicity, with a period of 25.5 h. Similar in-phase fluctuations were detected in constant darkness in C57BL/6NCrl mice (Figure 1D, middle), but not in arrhythmic Per1/2$^{-/-}$ mice (Figure 1D, right), suggesting that they reflect a circadian phenomenon. Our results were not biased by mouse age differences (Figure S1E). We detected a delay of ~3 h but a similar period when plotting the data against the ZT of the LTP-induction protocol (data not shown), suggesting that the local circadian machinery remains functional in slices. For consistency with previous work (Harris and Teyler, 1983), we used the ZT at which we sacrificed the mice and prepared tissue samples when describing other *in vitro* experiments. For the remainder of the experiments, we selected two time points representative of the L phase (ZT3.5) and D phase (ZT15.5). For simplicity, we refer to these times as the L and D phase, respectively. We detected LTP in the L and subjective L phases, but not in the D and subjective D phases (Figures 1E and 1F). There was no correlation between the magnitude of LTP and the stimulus intensity (r_L^2 = 0.01; r_D^2 = 0.47), and the results were not influenced by the choice of LTP-induction protocol,

(B) As in (A), but for the CA1-PC layer (*Arntl*: L, n = 28; D: n = 31; *Per2*: L, n = 31; D, n = 36). Data represent mean ± SEM.
(C) As in (A), but for *s.r.* (*Arntl*: L, n = 16; D, n = 17; *Per2*: L, n = 23; D, n = 31). Data represent mean ± SEM. Scale bar, 10 μm.
(D) Left: baseline-normalized fEPSP slope/FV amplitude in slices prepared at different ZTs (n = 23). Thick orange line, sinusoidal fit. Light orange bands, 95% confidence bands. Black/blue vertical lines, ZT3.5/15.5. Middle: as in left for C57BL/6NCrl mice in D/D (n = 67). Right: as in left for Per1/2$^{-/-}$ mice in D/D (n = 42).
(E) Top left: time course of baseline-normalized fEPSP slope/FV amplitude at ZT3.5 (L, black) and ZT15.5 (D, blue). Bottom left: as in top left for ZT3.5 (subjective L, magenta) and ZT15.5 (subjective D, purple) from mice kept in D/D. Right: average responses recorded in each condition 5 min before and 30 min after TBS. Each trace represents the average of 30 consecutive traces.
(F) Effect of TBS (L, n = 14; D, n = 7; subjective L, n = 19. subjective D, n = 10). The two rightmost bars were collected using tetanic stimulation (L, n = 11; D, n = 9). Data represent mean ± SEM.

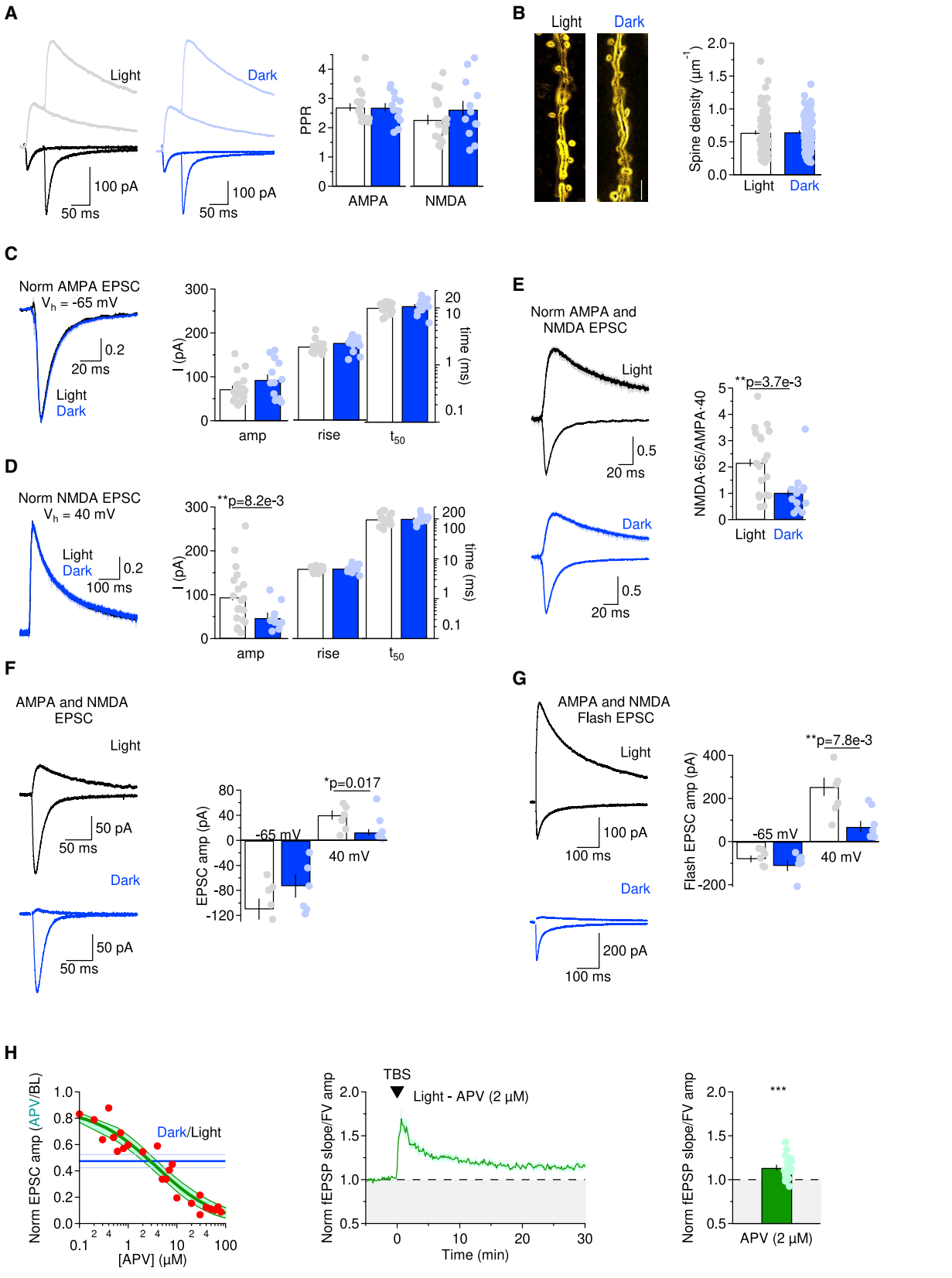

(legend on next page)

because the magnitude of LTP induced by tetanic stimulation was also larger in the L phase (Figure 1F).

In all of these experiments, we measured LTP using the ratio between the slope of the field excitatory postsynaptic potential (fEPSP) and the fiber volley (FV) amplitude. This approach allows us to minimize potential errors in the estimates of LTP arising from (1) trial-to-trial variability in the recruitment of pre-synaptic afferents due to the stochastic nature of voltage-gated sodium and potassium channel gating (O'Donnell and van Rossum, 2014), (2) nonlinear effects that this has on neurotransmitter release (Dodge and Rahamimoff, 1967), (3) small fluctuations in the tip resistance of the recording electrode, and (4) variability in the number of afferent fibers recruited across slices. This approach did not introduce factual errors in our measure of LTP, because the results remained qualitatively similar when using the fEPSP slope as a measure of LTP (Figures S1F and S1H–S1J).

We asked whether the circadian modulation of synaptic plasticity at Schaffer collateral synapses could be due to daily fluctuations in extracellular levels of D-serine, a co-agonist of NMDA receptors (Papouin et al., 2017). Consistent with our own previous studies (Scimemi et al., 2004, 2009), D-serine (50 μM) did not potentiate the NMDA excitatory postsynaptic current (EPSC) amplitude in CA1-PCs (Figure S1G), indicating that the circadian modulation of LTP is not due to changes in the activation of the NMDA receptor glycine-binding site.

The Surface Expression of NMDA Receptors on CA1-PCs Varies with Circadian Rhythmicity

We asked whether the loss of LTP in the D phase could be accounted for by changes in pre- or post-synaptic function (Figure 2). Our measures of AMPA and NMDA EPSC paired-pulse ratio (PPR) remained similar in the L/D phases, suggesting that there was no change in pre-synaptic release probability (Figure 2A). In these experiments, the stimulus strength was set to evoke AMPA EPSCs of similar amplitude in the L/D phases, and their rise and half-decay time were similar, suggesting no change in the time course of AMPA receptor activation (Figure 2C). The amplitude of the NMDA EPSCs, however, was smaller in the D phase, with no change in their rise and half-decay time (Figure 2D). This led to reduced NMDA/AMPA ratio in the D phase (Figure 2E), a result that we confirmed with RuBi-glutamate uncaging experiments. We recorded electrically evoked and flash-evoked AMPA and NMDA EPSCs in the same cells (Figures 2F and 2G). The amplitude of electrically and flash-evoked NMDA EPSCs was smaller in the D phase (Figure 2F), whereas that of AMPA EPSCs did not change (Figure 2G). These effects were not associated with overt changes in the density of excitatory synapses onto CA1-PCs, as the spine density in CA1-PC dendrites was similar in the L/D phases (Figure 2B).

If the loss of LTP in the D phase is due to reduced NMDA receptor expression (~53%), then we should occlude LTP in the L phase by blocking NMDA receptors by 53%. This can be achieved using D,L-2-amino-5-phosphonopentanoic acid (APV) (2 μM; Figure 2H, left). Despite this partial block of NMDA receptors, TBS could still induce LTP in APV (2 μM; Figure 2H, middle and right), suggesting that other mechanisms, in addition to loss of NMDA receptors, contribute to the circadian modulation of synaptic plasticity at Schaffer collateral synapses.

Circadian Changes in Astrocyte Glutamate Clearance Affect the Temporal Summation of AMPA EPSCs

On its own, the circadian reduction in the synaptic weight of NMDA currents is not expected to change the summation of AMPA or NMDA EPSCs evoked by temporally clustered stimuli, like those that compose each burst of the LTP-inducing TBS stimulation. Surprisingly, however, our experiments showed that the summation of AMPA EPSCs was reduced in the D phase (Figure 3A, top), with no significant effect on that of NMDA EPSCs (Figure 3A, bottom). Using a kinetic model of AMPA and NMDA receptors, we showed that these effects could be recapitulated by a prolongation in the lifetime of glutamate in the extracellular space, which would prolong the recovery time of AMPA receptors from the open to the closed state (Figure 3B). This hypothesis was supported by a multi-compartmental NEURON model, which takes into account the complex morphology of CA1-PCs and the random spatial distribution of excitatory inputs along dendrites (Figures 3C and 3D). In this model, the smaller AMPA EPSC summation in the D phase could be accounted for by a 3-fold increase in the recovery rate of the peak conductance of AMPA receptors (from 10 to 30 ms). The small reduction in NMDA EPSC summation in the D phase

Figure 2. NMDA Receptor Activation in CA1-PCs Is Reduced during the Dark Phase

(A) Left: example of single and paired AMPA and NMDA EPSCs. Each trace is the average of 20 stimulations. Right: AMPA and NMDA EPSC PPR (L, n = 19; D, n = 12). Data represent mean ± SEM.

(B) Left: biocytin-filled dendrites of CA1-PCs in the L/D phases. The confocal images were converted into maximum intensity projections and processed with a Canny-Deriche filtering for edge detection. Right: spine linear density (L, n = 85; D, n = 105). Data represent mean ± SEM. Scale bar, 10 μm.

(C) Peak-normalized AMPA EPSCs, with a summary of AMPA EPSC amplitude and kinetics (L, n = 19; D, n = 13). Data represent mean ± SEM.

(D) As in (C), but for NMDA EPSCs (L, n = 19; D, n = 13). Data represent mean ± SEM.

(E) Left: average AMPA and NMDA EPSCs, normalized by the peak of the AMPA current in each cell. Right: NMDA/AMPA ratio measures (L, n = 19; D, n = 13). Data represent mean ± SEM.

(F) Left: average electrically evoked AMPA and NMDA EPSCs recorded from CA1-PCs in the presence of RuBi-glutamate (L, n = 5; D, n = 5). Data represent mean ± SEM.

(G) Average flash-evoked AMPA and NMDA EPSCs recorded from CA1-PCs in response to RuBi-glutamate uncaging (L, n = 5; D, n = 5). Data represent mean ± SEM.

(H) Left: titration curve for APV on NMDA EPSC amplitude (n = 24). Thick green line and shaded areas represent the Hill fit of the data and 95% confidence bands, respectively. Horizontal blue and light blue lines represent the reduction of NMDA receptor activation detected in the D phase (see E). APV (2 μM) reduces the NMDA EPSC amplitude by 53%. Middle: time course of baseline-subtracted fEPSP slope/FV amplitude ratio in the presence of APV (2 μM) in the L phase. Right: effect of APV (2 μM) on LTP in the L phase (n = 19). Data represent mean ± SEM.

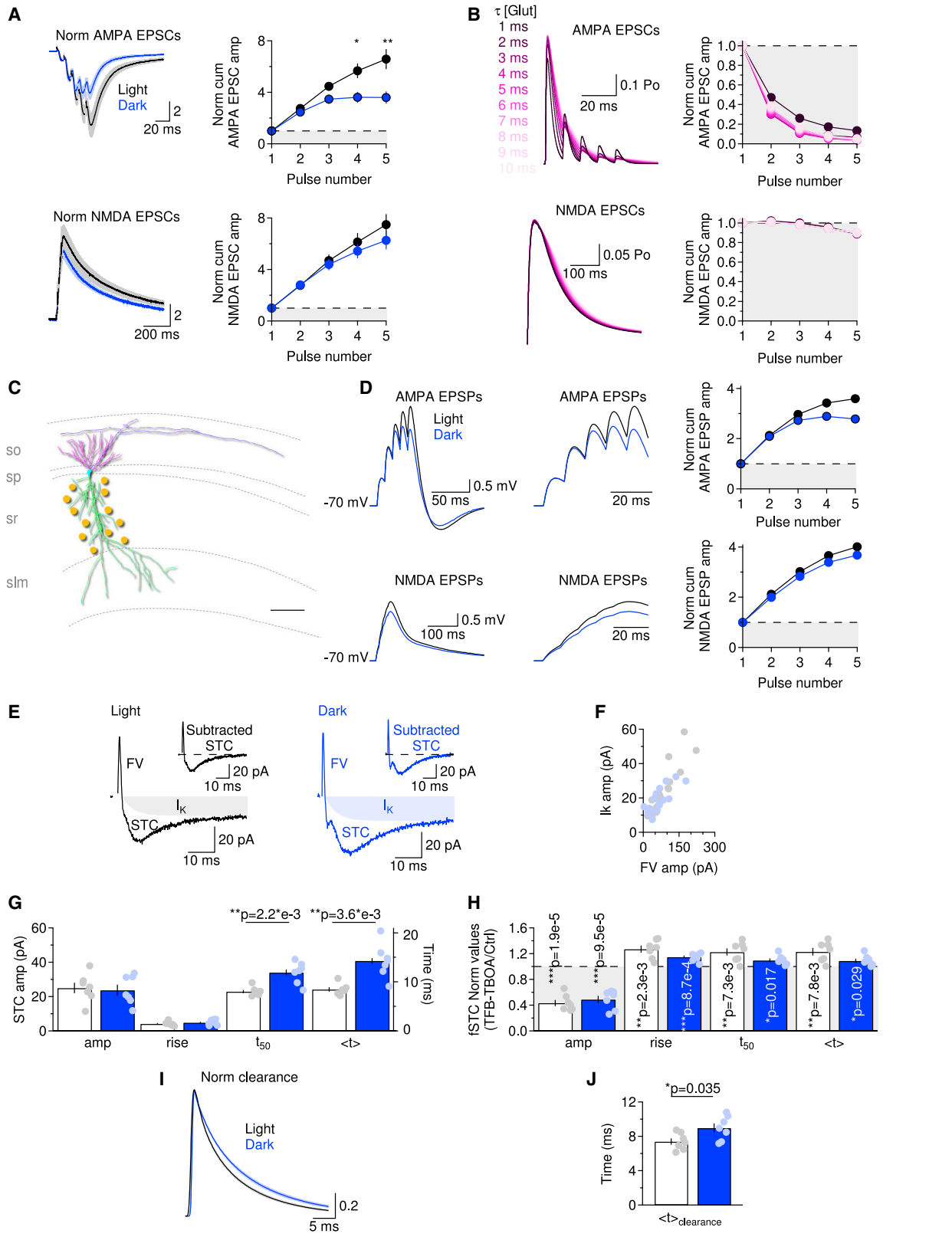

(legend on next page)

(Figure 3A) could be accounted for by a small, 15% reduction in the peak conductance of NMDA receptors, which does not lead to a significant change in the temporal summation of NMDA excitatory postsynaptic potentials (EPSPs) (Figure 3D).

In separate simulations, we changed the conductance of various ion channels to determine if these could explain the changes in the temporal summation of EPSPs between the L and D phases. We examined the role of high-and low-voltage-activated calcium channels (HVA and LVA, respectively), hyperpolarization-activated cation channels (I_h), and A-type potassium channels (I_{KA}; Figure S2). According to the model, a reduction in the temporal summation of EPSPs could occur if there was a 250-fold increase in the current density of HVA and LVA calcium channels (Figures S2A and S2C), a 3.3-fold increase in I_h (Figure S2E), or a 5-fold increase in I_{KA} channels (Figure S2G), but none of these changes were detected experimentally (Figures S2B, S2D, S2F, and S2H). For example, 4-aminopyridine (4AP), an antagonist of I_{KA} channels, increased the action potential duration without altering the action potential peak in the L/D phase (Figures S2I–2L). A 35-fold increase in the magnitude of delayed rectifier potassium currents (I_{KDR}; Figure S2M) or a 25-fold increase in calcium-activated potassium currents (I_{KCa}; Figure S2N) could also reduce the EPSP summation, but these effects are also expected to change the action potential waveform in the L/D phase, and this was not the case in our experiments (Figure S2I–S2L).

If the lifetime of synaptically released glutamate in the extracellular space is prolonged in the D phase, then the time course of synaptically activated glutamate transporter currents (STCs) in astrocytes should be slower. Schaffer collateral stimulation evokes glutamate release in *s.r.* and a complex current waveform in astrocytes (Diamond, 2005; Scimemi and Diamond, 2013; Scimemi et al., 2009; Sweeney et al., 2017). This is composed of a fast outward current (the FV) and a slower inward current representing the overlay of a sustained potassium current and the STC (Figure 3E). As expected, small changes in the stimulation strength across cells led to proportionate changes in the amplitude of the FV and the sustained potassium current (Figure 3F). The range of stimulus intensity used in our experiments evoked STCs of similar amplitude and rise time in the L/D phases, which decayed more slowly in the D phase (Figure 3G). The kinetics of the STC are similar to those of the facilitated portion of the STC (fSTC), obtained by subtracting STCs evoked by single and paired stimulation, which is used to derive the time course of glutamate clearance from astrocytes (Diamond, 2005; Scimemi and Diamond, 2013; Scimemi et al., 2009, 2013; Sweeney et al., 2017). The first step in this analysis requires recording STCs in the presence of a low concentration of the broad spectrum glutamate transporter antagonist 3S)-3-[[3-[[4-(trifluoromethyl)benzoyl]amino]phenyl]methoxy]-L-aspartic acid (TFB-TBOA) (1 μM), which reduced the fSTC amplitude and prolonged its kinetics similarly in the L/D phases (Figure 3H). The fSTC analysis showed that the time course of glutamate clearance from astrocytes was slower in the D phase, suggesting that the glutamate uptake capacity of astrocytes varies with time of day (Figures 3I and 3J).

The results of this analysis were not confounded by changes in the passive membrane properties of astrocytes (Figures S3A–S3D) and CA1-PCs in the L/D phases (Figure S3E). The astrocytes' resting membrane potential remained similar in the L/D phases (Figure S3F), as did their level of biocytin coupling (Figure S3F).

The slower glutamate clearance in the D phase was not due to reduced expression of the astrocyte glutamate transporters GLAST and GLT1, which we measured using western blotting (Figures 4A and 4B). A potential limitation of these experiments lies in the fact that this analysis was performed on all membrane-associated proteins, including those in the membrane of intracellular organelles. In reality, only glutamate transporters incorporated into the plasma membrane contribute to extracellular glutamate clearance. To address this concern, we used an *in vitro* surface biotinylation assay to measure the relative expression of GLAST and GLT1 in the L/D phases (Figures S4A–S4D) (Thomas-Crusells et al., 2003). This approach provided a reliable tool to separate transporters expressed in the plasma membrane from those trafficking through intracellular organelles, as indicated by the absence of biotinylated GLAST/GLT1 in the cytoplasmic fraction of our protein extracts (Figures S4B and S4D). These experiments confirmed that the relative expression of GLAST and GLT1 on the plasma membrane did not change in the L/D phases (Figures S4A and S4C).

The Gross Structure of the Hippocampal Neuropil Does Not Change during the Circadian Cycle

Other potential mechanisms that could account for the slower glutamate clearance in the D phase are widespread changes in

Figure 3. AMPA EPSC Summation and Extracellular Glutamate Clearance Are Reduced during the D Phase

(A) Top: train of AMPA EPSCs. Bottom: as in the top panel, but for NMDA EPSCs (L, n = 9; D, n = 7). Data represent mean ± SEM

(B) Top: ChanneLab simulations of AMPA EPSCs evoked by five consecutive glutamate release events (peak glutamate concentration, 1 mM; inter-pulse interval, 10 ms) using the kinetic scheme from Jonas et al. (1993). Bottom: as in the top panel, but for NMDA EPSCs using the kinetic scheme from Lester and Jahr (1992).

(C) Morphology of the biocytin-filled CA1-PC used to run NEURON simulations (soma, cyan; basal dendrites, magenta; apical dendrites, green; axon, purple; synaptic inputs in *s.r.*, *yellow*). Scale bar, 100 μm.

(D) Results of the NEURON multi-compartmental model. Top left: somatic AMPA EPSPs evoked by activating 100 synapses randomly distributed through the CA1-PC dendritic tree. Top middle: expanded timescale. Top right: normalized cumulative AMPA EPSP amplitude for the NEURON model. Bottom: as in the top panel, but for synapses containing only NMDA receptors.

(E) Example of whole-cell astrocyte recordings in the presence of the $GABA_A$ and AMPA receptor antagonists.

(F) The amplitude of I_Ks scaled with the FV amplitude (L, n = 19; D, n = 13).

(G) STC amplitude and kinetics (L, n = 7; D, n = 7). Data represent mean ± SEM.

(H) fSTC amplitude and kinetics (L, n = 7; D, n = 7). Data represent mean ± SEM.

(I) Average astrocyte glutamate clearance waveforms (L, n = 7; D, n = 7). Data represent mean ± SEM.

(J) Glutamate clearance centroids (L, n = 7; D, n = 7). Data represent mean ± SEM.

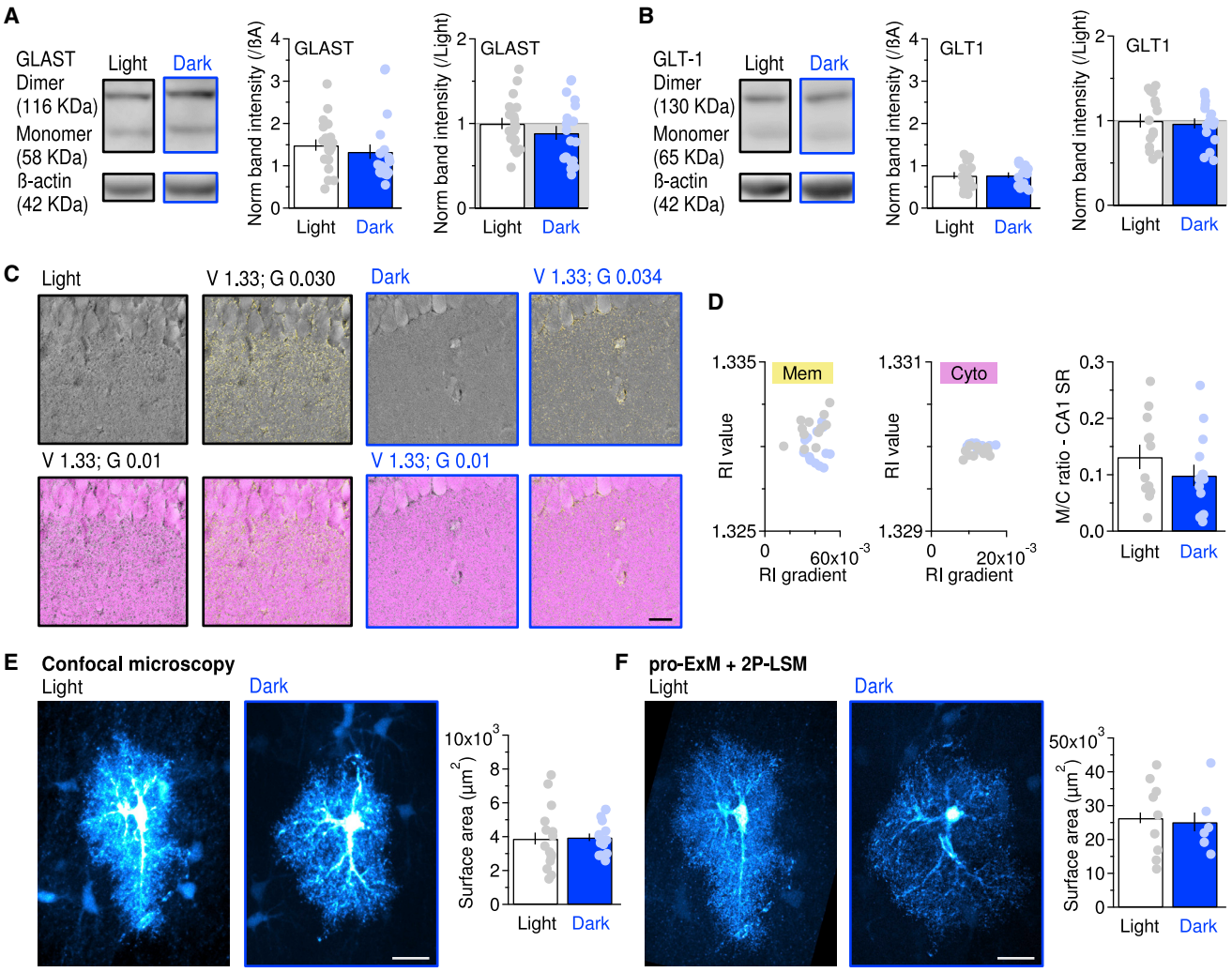

Figure 4. Glutamate Transporter Expression and Astrocyte Neuropil Coverage Are Not Altered in the L/D Phases

(A) Left: western blot analysis of hippocampal GLAST expression. Middle: GLAST band intensity, normalized to the corresponding intensity of β-actin. Right: data are further normalized by the band intensity in the L phase (L, n = 19; D, n = 20). Data represent mean ± SEM.

(B) As in (A), but for GLT1 (L, n = 15; D, n = 16). Data represent mean ± SEM.

(C) Example images collected from slices digitally stained using refractive index (RI) value (V) and gradient (G) combinations labeling cell membranes (yellow) and cytoplasm (magenta). Scale bar, 20 µm.

(D) Left: combinations of RI value and gradient used to label cell membranes. Middle: as in the left panel, but for the cytoplasm. Right: membrane to cytoplasm (M/C) ratio in *s.r.* (L, n = 12; D, n = 14). Data represent mean ± SEM.

(E) Maximum intensity projection of biocytin-filled astrocytes collected using confocal microscopy, with a summary of the astrocyte 2D surface area (L, n = 15; D, n = 17). Data represent mean ± SEM. Scale bar, 20 µm.

(F) Maximum intensity projection of the same astrocytes after proExM collected using 2P-LSM, with a summary of the astrocyte 2D surface area (L, n = 9; D, n = 6). Data represent mean ± SEM. Scale bar, 70 µm.

the structure of the neuropil caused by cell swelling or shrinkage. Alternatively, there could be more subtle, local rearrangements of the synaptic environment (Sweeney et al., 2017). We analyzed the cell membrane and cytoplasm composition of hippocampal slices using a marker-free holo-tomographic approach that distinguishes plasma membranes from cytoplasmic compartments based on their refractive index value and gradient (Cotte et al., 2013). This approach detects changes in the plasma membrane/cytoplasm (M/C) ratio caused by storing hippocampal slices in solutions of different osmolality (Figures S4E–S4H) in the CA1-PC layer (Figure S4G) and *s.r.*, where the M/C ratio was larger due to the absence of cell bodies (Figure S4H). The lack of difference between the measures obtained in the L/D phases suggests that no major cell swelling/shrinking occurs in the *s.r.* in the L/D phases (Figures 4C and 4D).

Though valuable, this analysis cannot identify structural changes that might occur only in astrocytes. To test this, we acquired confocal images of biocytin-filled astrocytes and analyzed their maximal intensity projections before and after protein-retention expansion microscopy (proExM), to overcome

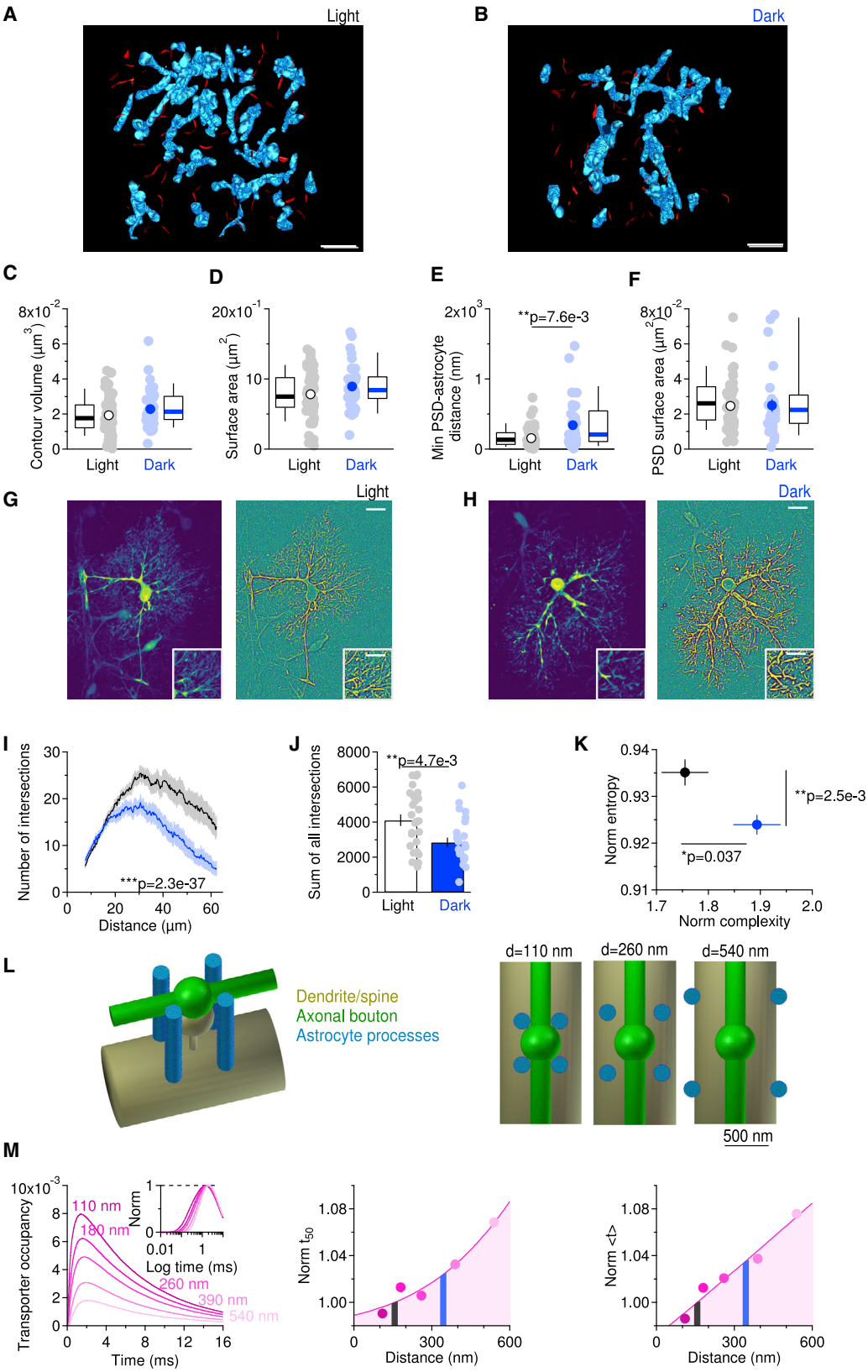

(legend on next page)

the caveat that the spatial resolution of confocal microscopy can be larger than the size of astrocytes' distal processes ($res_{x,y} = \lambda / 2 \cdot NA = 488/2 \cdot 1.4 = 174$ nm) (Tillberg et al., 2016). We subjected hippocampal slices collected in the L/D phases to three, 15-min rounds of expansion (Figure S5A), which lead to a ~3.5-fold increase in slice area (Figures S5B–S5D) and a ~2-fold increase in slice perimeter (Figures S5E–S5G). Before and after expansion, the biocytin-filled astrocytes showed similar surface area in the L/D phases (Figures 4E, 4F, S5H, and S5I), suggesting that the gross morphology of these cells does not change during the circadian cycle.

Astrocytes Reduce the Number of Their Fine Processes in the D Phase of the Circadian Cycle

The data outlined above do not rule out the possibility of more subtle changes in astrocytes' morphology, which can be resolved using 3D axial scanning transmission electron microscopy (STEM) tomography (Sousa et al., 2011; Sweeney et al., 2017). With this approach, we detected fewer astrocytic processes in the D phase (Figures 5A and 5B), with similar volume and surface area (Figures 5C and 5D). This led to a ~2-fold increase in the nearest-neighbor distance between each post-synaptic density (PSD) and the closest astrocyte process (from 155 ± 18 nm to 342 ± 63 nm) in the D phases (Figure 5E), with no change in PSD size (Figure 5F).

A common way to analyze the number of dendritic branches formed by neurons relies on the use of Sholl analysis. This analysis is prone to errors when used on nonprocessed confocal images of astrocytes because of the multitude and fuzziness of the fine processes of these cells. Information about these filamentous processes can be extracted using coherence-enhancing diffusion filtering (Weickert and Scharr, 2002) and an iterative convolution with oriented filters (Figures 5G and 5H). The Sholl analysis, applied to the processed confocal images, showed that the number of astrocytic intersections decreased in the D phase (Figures 5I and 5J). An alternative analytical method that relies on the use of a shearlet multiscale framework (Guo and Labate, 2007) provides an optimal approximation of anisotropic features, like astrocytic process in confocal images (Brazhe, 2018). This method uses spatial entropy and complexity to describe the orderliness and feature-preferred orientation of an image after normalizing their values by those obtained in the neuropil adjacent the biocytin-filled astrocyte. Consistent with the 3D axial STEM tomography and Sholl analysis, the normalized entropy was smaller in the D phase (Figure 5K) (Brazhe, 2018; Gavrilov et al., 2018), indicating that astrocytes remodel their processes during the circadian cycle. We ran 3D Monte Carlo reaction-diffusion simulations to confirm that changes in the astrocyte-PSD distance could change the time course of STCs. Accordingly, changing the astrocyte-PSD distance within the range detected in the tomography reconstructions prolonged the glutamate transporter occupancy, slowing down the time course of STCs and of glutamate clearance from the extracellular space (Figures 5L and 5M).

Neurons and Astrocytes Cooperate to Mediate Circadian Changes in Excitatory Synaptic Transmission

Although our experiments show that the structural and functional properties of hippocampal astrocytes change during the circadian cycle, it is not clear whether this effect, on its own, accounts for the loss of LTP in the D phase. We tested this hypothesis using the positive allosteric modulator of AMPA receptors LY404187 (Quirk and Nisenbaum, 2002). At concentrations greater than 0.02 μM, LY404187 induced a maximal potentiation of the AMPA EPSC amplitude and decay (Figure 6A, top) and reduced the AMPA EPSC summation in the L phase to levels similar to those detected in the D phase (cf. Figure 6A, bottom, and Figure 2A). Does this pharmacological manipulation occlude LTP in the L phase? LY404187 (0.02 μM) did not alter LTP in the L phase (Figure 6B, top), suggesting that the prolonged activation and reduced temporal summation of AMPA EPSCs are not the sole mechanisms accounting for loss of LTP in the D phase. However, TBS-induced LTP in the L phase was blocked in the presence of both APV (2 μM) and LY404187 (0.02 μM), suggesting that both neurons and astrocytes contribute to this effect (Figure 6B, bottom).

Novel Object Recognition, but Not Memory of Familiar Environments, Is Susceptible to Circadian Modulation

The biophysical model of CA1-PCs (Figures 3B–3D) showed that decreased NMDA receptor expression and increased recovery

Figure 5. Astrocytes Reduce the Number of Their Fine Processes in the D Phase, Leading to Slower Glutamate Clearance

(A and B) 3D axial STEM tomography reconstruction of hippocampal astrocytic processes (blue) and PSDs (red) in *s.r.* in the L and D phases. Scale bar, 1 μm.

(C) Astrocytic processes volume (L, n = 73; D, n = 37). White and blue dots represent the mean ± SEM. Box and whisker plots show the median, 25th–75th percentile, and 10th–90th percentile.

(D) As in (C), but for astrocytic processes surface area.

(E) As in (C), but for distance measures between PSDs and their nearest neighboring astrocyte (L, n = 59; D, n = 32).

(F) As in (C), but for PSD surface area.

(G) Left: maximum intensity projection of pre-processed confocal z stacks. Right: segmentation of the projection for Sholl analysis with probabilistic thresholding. Scale bar, 10 μm. Inset scale bar, 20 μm.

(H) As in (G), but for biocytin-filled neurons in the D phase.

(I) Sholl analysis of astrocyte branching (L, n = 14; D, n = 18). Data represent mean ± SEM.

(J) Total number of intersections measured by the Sholl analysis (L, n = 26; D, n = 20). Data represent mean ± SEM.

(K) Entropy and complexity values for each cell, normalized by the corresponding values in the neuropil around them (L, n = 29; D, n = 16). Data represent mean ± SEM.

(L) Left: 3D representation of the synaptic environment, including an axonal bouton (green), a spine with its parent dendrite (gold), and four adjacent astrocytic processes (blue). Right: top view of the synaptic environment with astrocyte processes positioned at increasing distance from the PSD.

(M) Left: glutamate transporter occupancy following the release of 2,000 glutamate molecules. Inset: peak-normalized traces. Middle: normalized half-decay time of glutamate transporter occupancy obtained at varying astrocyte-PSD distances. Black and blue lines represent values of astrocyte-PSD distance measured in the tomography analysis (see E). Right: as in the middle panel, but for centroids.

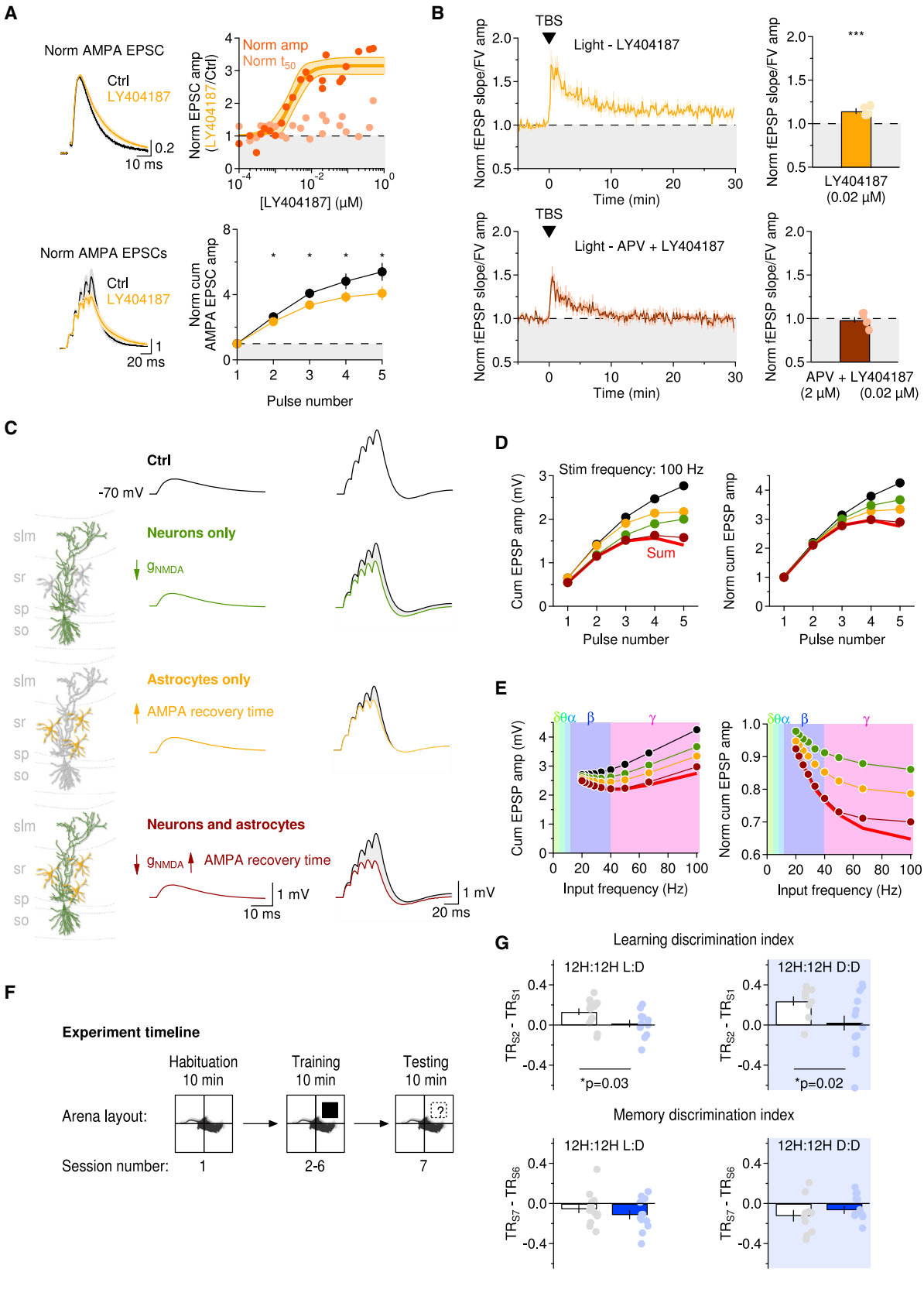

(legend on next page)

time from activation of AMPA receptors alter the summation of composite glutamatergic EPSPs at stimulation frequencies in the β-γ range (Figures 6C–6E). A further reduction in temporal summation was observed when both manipulations were performed at the same time. Their effects summate linearly in the β and slow γ frequency range (<50 Hz) and sublinearly for inputs in the fast γ range (65–100 Hz).

These results are relevant in the context of hippocampal-dependent cognition and exploratory behaviors. In hippocampal area CA1, slow γ oscillations synchronize with slow γ activity in area CA3 during exploration of familiar environments and memory recall (Colgin et al., 2009). By contrast, fast γ activity synchronizes with fast γ activity in entorhinal cortex during novel object recognition and learning (Zheng et al., 2016) through activation of nonuniformly distributed dendritic ionic conductances (Combe et al., 2018). According to our model, hippocampal activity in the high γ range is most susceptible to circadian modulation, whereas the integration of inputs at lower frequency ranges is less affected. If this were true, then we would expect behaviors that rely on high-frequency hippocampal activity, like learning and exploration of novel environments, to vary with the time of day. By contrast, memory recall and exploration of familiar environments, which rely on hippocampal activity at lower frequencies, should be less susceptible to circadian modulation. We tested this hypothesis *in vivo* using a novel object recognition behavioral test on four cohorts of mice (two kept under 12 h:12 h L/D and trained and tested in the L or D phase, and two kept in constant darkness and trained and tested in the subjective L or subjective D phase; Figures 6F and 6G) (Antunes and Biala, 2012; Broadbent et al., 2009; Ennaceur and Delacour, 1988). During the first habituation session, we positioned a mouse in an open field arena and allowed it to freely explore it. In the following five training sessions, we reintroduced the mouse in the same arena, after positioning a nonfamiliar object in its top right corner, which we labeled with a visual cue. Then, on the last session, we removed the object (Figure 6F). We quantified object exploration by computing the learning and memory discrimination indexes from scores of the proportion of time that each mouse spent exploring the new object in the first and last training session, respectively (Figure 6G). There was a significant decrease in the learning discrimination index in mice trained and tested in the D and subjective D phases (Figure 6G, top). By contrast, the memory discrimination index remained similar between mice trained and tested in the L/D or subjective L/subjective D phases (Figure 6G, bottom). Therefore, learning, but not memory recall, shows the highest sensitivity to time of day.

The Role of Corticosterone

As a last step, we gained insights into the mechanisms accounting for the circadian modulation of receptor composition and activation at Schaffer collateral synapses. We reasoned that the circadian changes in LTP might be triggered by an increase in the circulating levels of corticosterone, a glucocorticoid produced by the adrenal cortex and brain cells mostly in the active phase (i.e., D phase in mice) (Diotel et al., 2018). Using a radioimmunoassay, we confirmed that changes in the blood levels of corticosterone occur in juvenile mice aged P14–P21 in L/D and D/D (Figure 7A). Molecules with low molecular weight, like corticosterone (346 g), glutamate (147 g), and GABA (103 g), are not fully washed out from slice preparations and give rise to sustained receptor activation (Brickley et al., 1996; Scimemi et al., 2005; Semyanov et al., 2003, 2004; Stell et al., 2003). If the circadian changes in LTP were due to higher activation of corticosteroid receptors in the D phase, then blocking them pharmacologically should rescue LTP in the D phase without altering it in the L phase. Consistent with this hypothesis, blocking NR3C1/2 receptors did not occlude LTP in the L phase (Figures 7B and 7C) but rescued LTP in the D phase (Figures 7D and 7E). C57BL/6 mice carry two mutations in biosynthetic enzymes for melatonin (Ebihara et al., 1986; Kasahara et al., 2010; Peirson et al., 2018), and MT1/2 receptor gene expression is low in the hippocampus (Saunders et al., 2018). Accordingly, blocking MT1/2 receptors in the L phase did not occlude LTP (Figures 7B and 7C) and did not rescue LTP in the D phase (Figures 7D and 7E). Is the rescue of LTP detected by blocking NR3C1/2 receptors in the D phase due to a rescue of NMDA receptor expression and AMPA receptor activation? We showed that the NMDA/AMPA ratio of EPSCs evoked by flash uncaging RuBi-glutamate was larger in slices prepared in the D phase and treated with NR3C1/2, but not MT1/2, antagonists (Figure 7F). Likewise, the temporal summation of AMPA EPSCs in

Figure 6. Astrocytes and Neurons Cooperate to Mediate Frequency-Dependent Circadian Changes in Synaptic Integration

(A) Top left: peak-normalized AMPA EPSCs in control conditions and in LY404187 (0.02 μM; n = 15 cells). Top right: titration for the effect of LY404187 on AMPA EPSC amplitude (red dots) and half-decay time (t_{50}, yellow dots) in the L phase. Thick orange line and shaded areas represent Hill fit of the amplitude data and 95% confidence bands, respectively. Bottom left: train of AMPA EPSCs. Bottom right: effect of LY404187 (0.02 μM) on AMPA EPSC summation.

(B) Top: time course and statistical summary of baseline-subtracted fEPSP slope/FV amplitude ratio in the L phase, in LY404187 (0.02 μM; n = 9). Bottom: as in the top panel, but in LY404187 (0.02 μM) and APV (2 μM; n = 8). Data represent mean ± SEM.

(C) NEURON simulations of composite AMPA an NMDA EPSPs evoked using the realistic model of a CA1-PC shown in Figure 3C. The simulations were run to mimic glutamatergic EPSPs during the L phase (black) and in conditions that mimic the reduced NMDA receptor expression in the D phase (green), the reduced AMPA EPSP summation during the D phase due to retraction of astrocytic processes (yellow), or both effects at the same time (brown).

(D) Left: cumulative EPSP amplitude obtained from the model when delivering five pulses at 100 Hz. The red line represents the arithmetic sum of the effect introduced by reducing the NMDA receptor conductance (green) and increasing the recovery time of AMPA receptors (yellow). Simulations run when combining these effects are in brown. Right: as in the left panel, but after normalizing the data by the peak of the first EPSP.

(E) Results of NEURON simulations obtained in response to stimulations at different frequencies. Left: cumulative glutamatergic EPSP amplitude. Right: cumulative EPSP amplitude, obtained by normalizing the peak depolarization after the fifth stimulus by the amplitude of the first EPSP.

(F) Experimental timeline for novel object recognition test.

(G) Learning and memory discrimination index in mice maintained on 12 h:12 h L/D (left) and D/D (right). Mice were trained and tested either in the L or D phase (left) or the subjective L or subjective D phase (right). TF, proportion of time spent in the top right corner of the arena (learning: L, n = 14; D, n = 12; subjective L, n = 10; subjective D, n = 16; memory: L, n = 14; D, n = 12; subjective L, n = 10; subjective D, n = 16). Data represent mean ± SEM.

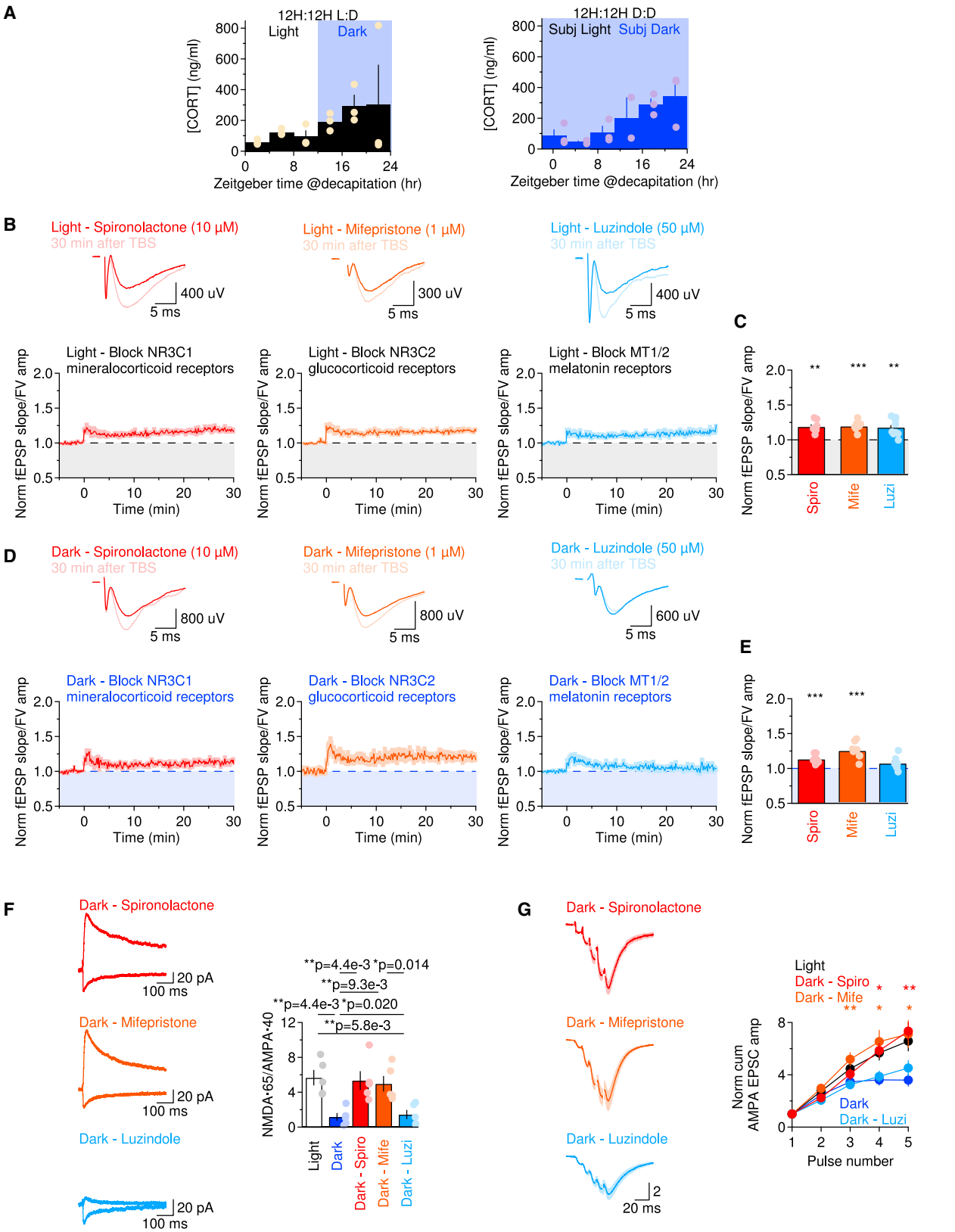

(legend on next page)

slices prepared in the D phase and treated with NR3C1/2, but not MT1/2, antagonists was similar to that recorded in the L phase (Figure 7G). These data identify corticosterone and corticosteroid receptors as key players in the circadian modulation of synaptic strength at Schaffer collateral synapses.

DISCUSSION

Astrocytes, Neurons, and the Values of an Ever-Changing Brain

Modifications of the synaptic environment are critical for information coding in the brain and provide an important substrate for circuit plasticity. For example, there are activity-dependent changes in the shape, size, and turnover of dendritic spines (Engert and Bonhoeffer, 1999; Gilbert, 1998; Holtmaat et al., 2005; Kwon and Sabatini, 2011; Rakic et al., 1986; Richards et al., 2005). Analogous activity-dependent phenomena of structural plasticity occur in small protoplasmic astrocytic processes around synapses (Lavialle et al., 2011; Reichenbach et al., 2010), which extend and retract through the hippocampal and brainstem neuropil (Haber et al., 2006; Hirrlinger et al., 2004). In the SCN, these movements occur with circadian rhythmicity and over physiologically relevant distances, comparable to the distance that spines can grow or shrink (Becquet et al., 2008). What at first sight might seem like small changes in the relative proximity of astrocytic processes and spines have important consequences on the lifetime of glutamate in the extracellular space and ultimately regulate the strength and timing of information transfer across neurons. Accordingly, suppressing astrocyte motility impairs the stabilization and maturation of synapses (Nishida and Okabe, 2007).

There are multiple molecular mechanisms that can change the proximity of astrocytic processes to spines, including PAR1 G-protein-coupled receptor activation (Sweeney et al., 2017). The experiments described here indicate that astrocyte remodeling in the hippocampus occurs not only in experimental conditions mimicking pathological states but also daily under physiological conditions, in concert with changes in glutamate receptor activation in CA1-PCs. The reasons for this regular remodeling remain unclear. One hypothesis is that this may be a necessary step in a long-term investment plan, whereby tuning down synaptic efficacy in the D phase may bring the hippocampus into a low-energy-demanding state, to parse energy consumption over longer periods of time (Attwell and Laughlin, 2001). Alternatively, these fluctuations might allow hippocampal networks to switch between functioning modes that best process different types of information at specific time points during the day. According to Marr's theory of the archicortex, the hippocampus alternates between times during which it stores information about patterns of neural activity representing events as they happen and times during which this information is transferred to other regions of the brain, including the neocortex (Marr, 1971; Willshaw et al., 2015). For nocturnal animals like mice, the time to store information locally would be the L phase, whereas the time to relay information to the neocortex would be the active D phase. According to our experiments, hippocampal activity in the high γ range, associated with learning and memory encoding, is highly susceptible to circadian modulation. In contrast, hippocampal activity encoding episodic, semantic, and working memory information (θ, α, and β ranges) is much less affected by time of day.

In 1983, Harris and Teyler first reported that in juvenile and adult rats, LTP expression at hippocampal Schaffer collateral synapses is more robust in the L phase (Harris and Teyler, 1983). Since these results were obtained in reduced slice preparations, it was concluded that they did not depend on the activity of extra-hippocampal afferents but rather depended on the enduring effects of modulators that are retained in slice preparations. Similar conclusions were later obtained in hamsters (Raghavan et al., 1999). One of the first candidate molecules thought to mediate these effects was the hormone melatonin, mainly synthesized in the D phase in the pineal gland (Vanecek, 1998). In acute hippocampal slices, exogenously applied melatonin blocks LTP induction without altering low-frequency synaptic transmission (Collins and Davies, 1997; Wang et al., 2005). These effects are unlikely to be mediated by melatonin binding to melatonin receptors, because there are few melatonin receptors expressed in the hippocampus. Given that melatonin has close structural similarity to various antagonists of the glycine-binding site of NMDA receptors, it was hypothesized that melatonin might reduce LTP by antagonizing NMDA receptors (Huettner, 1989; Salituro et al., 1990, 1992), but this hypothesis was disputed by (Collins and Davies, 1997). If melatonin does not have any known membrane receptor target, then how does it exert its biological actions? Because of its hydrophobicity, melatonin released into the bloodstream can easily pass through cell membranes and modulate a variety of intracellular molecular pathways or bind to nuclear receptors (Benítez-King et al., 1996, 2001; Carlberg and Wiesenberg, 1995; Rafii-El-Idrissi et al., 1998). Some of these interactions could have a deleterious effect on LTP, but many inbred strains of laboratory mice, including C57BL/6, have no detectable levels of melatonin in the pineal gland due to two independent mutations in the genes encoding the biosynthetic enzymes for melatonin (Ebihara et al., 1986; Kasahara et al., 2010; Peirson et al., 2018). It is therefore

Figure 7. Blocking Corticosteroid Receptors Rescues LTP, NMDA Receptor Expression, and AMPA Receptor Activation in the D Phase

(A) Plasma corticosterone measured at baseline in mice kept under 12 h:12 h L/D (left, n = 18) and D/D (right, n = 17). Data represent mean ± SEM.

(B) Top: average responses recorded 5 min before and 30 min after TBS. Bottom: time course of baseline-subtracted ratio between the fEPSP slope and the FV amplitude in the L phase in the presence of spironolactone, mifepristone, and luzindole. Data represent mean ± SEM.

(C) Summary for the experiments in (B) (Spiro, n = 7; Mife, n = 8; Luzi, n = 11). Data represent mean ± SEM.

(D) As in (B), but for the D phase. Data represent mean ± SEM.

(E) Summary for the experiments shown in D (Spiro, n = 8; Mife, n = 8; Luzi, n = 7). Data represent mean ± SEM.

(F) Average flash-evoked AMPA and NMDA EPSCs recorded from CA1-PCs in response to RuBi-glutamate uncaging, after pre-incubating slices for >30 min with each antagonist (all conditions, n = 5). Data represent mean ± SEM.

(G) Train of AMPA EPSCs and summary (L, n = 9; D, n = 7; D Spiro, n = 7; D Mife, n = 10; D Luzi, n = 12). Data represent mean ± SEM.

unlikely that our circadian effects on astrocyte morphology and AMPA EPSC summation are mediated by melatonin acting on molecular targets aside from MT1/2 receptors, and our results do not support this hypothesis. In contrast, corticosterone is produced with circadian rhythmicity and acts by activating mineralocorticoid (type I) and glucocorticoid receptors (type II), abundantly expressed in the hippocampus and implicated with synaptic plasticity and memory formation (Chung et al., 2011; Kim and Yoon, 1998). Because of their different steady-state affinity, type I receptors are fully occupied at low glucocorticoid plasma levels, whereas type II receptors become fully occupied only with higher glucocorticoid plasma levels (Chung et al., 2011; Pavlides et al., 1995). Physiological increase in alertness in the D phase can activate both receptor types. Although the exclusive activation of type I receptors promotes LTP, the concomitant activation of type II receptors suppresses it (Pavlides et al., 1995). Consistent with these findings, our experiments show that loss of LTP in the D phase is associated with activation of type I–II receptors.

Since there are numerous molecular and behavioral differences and similarities between humans and mice, one needs to be cautious about making quick analogies across species. As a substantial reprogramming of oscillating transcripts occurs in temporal lobe epilepsy (Debski et al., 2017), our findings may have implications that advance our understanding not only of circadian rhythmicity during physiological conditions but also of the pathogenesis of this disease and other chronic diseases.

STAR★METHODS

Detailed methods are provided in the online version of this paper and include the following:

- KEY RESOURCES TABLE
- RESOURCE AVAILABILITY
  - Lead Contact
  - Materials Availability
  - Data and Code Availability
- EXPERIMENTAL MODEL AND SUBJECT DETAILS
  - C57BL/6NCrl line
  - Per1/2$^{-/-}$ line
- METHOD DETAILS
  - Genotyping
  - *In vivo* chronic temperature recordings
  - Fluorescent *in situ* hybridization of clock gene transcripts using RNAscope fluorescence *in situ* hybridization (FISH)
  - Acute slice preparation and electrophysiology recordings
  - Blood collection and corticosterone radioimmunoassay
  - Biocytin filling and confocal imaging
  - Protein-retention expansion microscopy and two-photon imaging
  - Western blot
  - Surface protein biotinylation assay
  - Electron microscopy and axial STEM tomography
  - Tomographic holographic 3D microscopy
  - NEURON modeling
  - CellBlender modeling
  - Data analysis
  - Image preprocessing for Sholl analysis
  - Image analysis of complexity and entropy
  - Novel object recognition test
- QUANTIFICATION AND STATISTICAL ANALYSIS

SUPPLEMENTAL INFORMATION

Supplemental Information can be found online at https://doi.org/10.1016/j.celrep.2020.108255.

ACKNOWLEDGMENTS

We would like to thank Drs. Pablo Valdes and Ed Boyden for support with the proExM protocol, Tyler A. Mitchell for support with biotynilation and behavior experiments, and Dr. Jennifer M. Hurley for her generous gift of Per1/2$^{-/-}$ mice. Thanks to Drs. Juan Burrone and Christophe Bernard for valuable discussions and Dr. Daniela Tropea for comments on the manuscript.

This work was supported by the Presidential Award for Undergraduate Research and Initiative for Women Award (N.A.); RFBR COMFI grant 17-00-00412K for joint research to A. Semyanov (grant 17-00-00409) and A.B. (grant 17-00-00407); the NIH/NIBIB Intramural Research Program (grant ZIAEB000046 to R.D.L.); NIH/NIDA grant R01DA04741001 (A.K.); NIH/NIMH grant R15MH118692 and the SUNY Albany and the SUNY Albany Research Foundation (D.G.Z.); the EU Horizon 2020 Framework Program for Research and Innovation (grants 785907 and 945539, Human Brain Project SGA2 and SGA3; M.M. and R.M.); and NSF grant IOS2011998, NIH/NINDS grant R03NS102822, and the SUNY Albany and SUNY Albany Research Foundation (A. Scimemi).

AUTHOR CONTRIBUTIONS

Conceptualization, A. Scimemi; Methodology, A.B. and A. Scimemi; Software: A.B., M.M., R.M., and A. Scimemi; Validation, A. Scimemi; Formal Analysis, J.P.M., M.A.P., L.Y.D., G.C.T., N.A., J.J.W., S.Z., S.S., A.A.S., D.G.Z., R.M., A. Scimemi; Investigation, J.P.M., M.A.P., L.Y.D., G.C.T., N.A., R.M.D.G., R.M., and A. Scimemi; Resources, R.D.L., A.K., A. Semyanov, M.M., and A. Scimemi; Data Curation, A. Scimemi; Writing – Original Draft, A. Scimemi; Writing – Review & Editing, A. Scimemi; Visualization, A. Scimemi; Supervision, A. Scimemi; Project Administration, A. Scimemi.

DECLARATION OF INTERESTS

The authors declare no competing interests.

Received: November 13, 2019
Revised: August 21, 2020
Accepted: September 18, 2020
Published: October 13, 2020

REFERENCES

Antunes, M., and Biala, G. (2012). The novel object recognition memory: neurobiology, test procedure, and its modifications. Cogn. Process. *13*, 93–110.

Attwell, D., and Laughlin, S.B. (2001). An energy budget for signaling in the grey matter of the brain. J. Cereb. Blood Flow Metab. *21*, 1133–1145.

Bae, K., Jin, X., Maywood, E.S., Hastings, M.H., Reppert, S.M., and Weaver, D.R. (2001). Differential functions of mPer1, mPer2, and mPer3 in the SCN circadian clock. Neuron *30*, 525–536.

Balsalobre, A., Brown, S.A., Marcacci, L., Tronche, F., Kellendonk, C., Reichardt, H.M., Schütz, G., and Schibler, U. (2000). Resetting of circadian time in peripheral tissues by glucocorticoid signaling. Science *289*, 2344–2347.

Barbour, B. (2001). An evaluation of synapse independence. J. Neurosci. *21*, 7969–7984.

Barnes, C.A., McNaughton, B.L., Goddard, G.V., Douglas, R.M., and Adamec, R. (1977). Circadian rhythm of synaptic excitability in rat and monkey central nervous system. Science *197*, 91–92.

Becquet, D., Girardet, C., Guillaumond, F., François-Bellan, A.M., and Bosler, O. (2008). Ultrastructural plasticity in the rat suprachiasmatic nucleus. Possible involvement in clock entrainment. Glia *56*, 294–305.

Benítez-King, G., Ríos, A., Martínez, A., and Antón-Tay, F. (1996). In vitro inhibition of Ca2+/calmodulin-dependent kinase II activity by melatonin. Biochim. Biophys. Acta *1290*, 191–196.

Benítez-King, G., Hernández, M.E., Tovar, R., and Ramírez, G. (2001). Melatonin activates PKC-alpha but not PKC-epsilon in N1E-115 cells. Neurochem. Int. *39*, 95–102.

Bergles, D.E., Tzingounis, A.V., and Jahr, C.E. (2002). Comparison of coupled and uncoupled currents during glutamate uptake by GLT-1 transporters. J. Neurosci. *22*, 10153–10162.

Brazhe, A. (2018). Shearlet-based measures of entropy and complexity for two-dimensional patterns. Phys. Rev. E *97*, 061301.

Brickley, S.G., Cull-Candy, S.G., and Farrant, M. (1996). Development of a tonic form of synaptic inhibition in rat cerebellar granule cells resulting from persistent activation of GABAA receptors. J. Physiol. *497*, 753–759.

Broadbent, N.J., Gaskin, S., Squire, L.R., and Clark, R.E. (2009). Object recognition memory and the rodent hippocampus. Learn. Mem. *17*, 5–11.

Buzsáki, G. (2002). Theta oscillations in the hippocampus. Neuron *33*, 325–340.

Carlberg, C., and Wiesenberg, I. (1995). The orphan receptor family RZR/ROR, melatonin and 5-lipoxygenase: an unexpected relationship. J. Pineal Res. *18*, 171–178.

Chaudhury, D., and Colwell, C.S. (2002). Circadian modulation of learning and memory in fear-conditioned mice. Behav. Brain Res. *133*, 95–108.

Chung, S., Son, G.H., and Kim, K. (2011). Circadian rhythm of adrenal glucocorticoid: its regulation and clinical implications. Biochim. Biophys. Acta *1812*, 581–591.

Clements, J.D., and Bekkers, J.M. (1997). Detection of spontaneous synaptic events with an optimally scaled template. Biophys J *73*, 220–229.

Colgin, L.L., Denninger, T., Fyhn, M., Hafting, T., Bonnevie, T., Jensen, O., Moser, M.B., and Moser, E.I. (2009). Frequency of gamma oscillations routes flow of information in the hippocampus. Nature *462*, 353–357.

Collins, D.R., and Davies, S.N. (1997). Melatonin blocks the induction of long-term potentiation in an N-methyl-D-aspartate independent manner. Brain Res. *767*, 162–165.

Combe, C.L., Canavier, C.C., and Gasparini, S. (2018). Intrinsic mechanisms of frequency selectivity in the proximal dendrites of CA1 pyramidal neurons. J. Neurosci. *38*, 8110–8127.

Cotte, Y., Toy, F., Jourdain, P., Pavillon, N., Boss, D., Magistretti, P., Marquet, P., and Depeursinge, C. (2013). Marker-free phase nanoscopy. Nat. Photonics *7*, 113–117.

Debski, K.J., Ceglia, N., Ghestem, A., Ivanov, A.I., Brancati, G.E., Bröer, S., Bot, A.M., Müller, J.A., Schoch, S., Becker, A., et al. (2017). The circadian hippocampus and its reprogramming in epilepsy: impact for chronotherapeutics. bioRxiv. https://doi.org/10.1101/199372.

Diamond, J.S. (2005). Deriving the glutamate clearance time course from transporter currents in CA1 hippocampal astrocytes: transmitter uptake gets faster during development. J. Neurosci. *25*, 2906–2916.

Diotel, N., Charlier, T.D., Lefebvre d'Hellencourt, C., Couret, D., Trudeau, V.L., Nicolau, J.C., Meilhac, O., Kah, O., and Pellegrini, E. (2018). Steroid transport, local synthesis, and signaling within the brain: roles in neurogenesis, neuroprotection, and sexual behaviors. Front. Neurosci. *12*, 84.

Dodge, F.A., Jr., and Rahamimoff, R. (1967). On the relationship between calcium concentration and the amplitude of the end-plate potential. J. Physiol. *189*, 90P–92P.

Dubocovich, M.L., Rivera-Bermudez, M.A., Gerdin, M.J., and Masana, M.I. (2003). Molecular pharmacology, regulation and function of mammalian melatonin receptors. Front. Biosci. *8*, d1093–d1108.

Ebihara, S., Marks, T., Hudson, D.J., and Menaker, M. (1986). Genetic control of melatonin synthesis in the pineal gland of the mouse. Science *231*, 491–493.

Engert, F., and Bonhoeffer, T. (1999). Dendritic spine changes associated with hippocampal long-term synaptic plasticity. Nature *399*, 66–70.

Ennaceur, A., and Delacour, J. (1988). A new one-trial test for neurobiological studies of memory in rats. 1: Behavioral data. Behav. Brain Res. *31*, 47–59.

Gasparini, S., Migliore, M., and Magee, J.C. (2004). On the initiation and propagation of dendritic spikes in CA1 pyramidal neurons. J. Neurosci. *24*, 11046–11056.

Gavrilov, N., Golyagina, I., Brazhe, A., Scimemi, A., Turlapov, V., and Semyanov, A. (2018). Astrocytic Coverage of Dendritic Spines, Dendritic Shafts, and Axonal Boutons in Hippocampal Neuropil. Front. Cell. Neurosci. *12*, 248.

Gerstner, J.R., Lyons, L.C., Wright, K.P., Jr., Loh, D.H., Rawashdeh, O., Eckel-Mahan, K.L., and Roman, G.W. (2009). Cycling behavior and memory formation. J. Neurosci. *29*, 12824–12830.

Gilbert, C.D. (1998). Adult cortical dynamics. Physiol. Rev. *78*, 467–485.

Guilding, C., and Piggins, H.D. (2007). Challenging the omnipotence of the suprachiasmatic timekeeper: are circadian oscillators present throughout the mammalian brain? Eur. J. Neurosci. *25*, 3195–3216.

Guo, K., and Labate, D. (2007). Optimally sparse multidimensional representation using shearlets. SIAM J. Math. Anal. *39*, 298–318.

Haber, M., Zhou, L., and Murai, K.K. (2006). Cooperative astrocyte and dendritic spine dynamics at hippocampal excitatory synapses. J. Neurosci. *26*, 8881–8891.

Harris, K.M., and Teyler, T.J. (1983). Age differences in a circadian influence on hippocampal LTP. Brain Res. *261*, 69–73.

Hines, M.L., and Carnevale, N.T. (1997). The NEURON simulation environment. Neural Comput. *9*, 1179–1209.

Hirrlinger, J., Hülsmann, S., and Kirchhoff, F. (2004). Astroglial processes show spontaneous motility at active synaptic terminals in situ. Eur. J. Neurosci. *20*, 2235–2239.

Hohmann-Marriott, M.F., Sousa, A.A., Azari, A.A., Glushakova, S., Zhang, G., Zimmerberg, J., and Leapman, R.D. (2009). Nanoscale 3D cellular imaging by axial scanning transmission electron tomography. Nat. Methods *6*, 729–731.

Holtmaat, A.J.G.D., Trachtenberg, J.T., Wilbrecht, L., Shepherd, G.M., Zhang, X., Knott, G.W., and Svoboda, K. (2005). Transient and persistent dendritic spines in the neocortex in vivo. Neuron *45*, 279–291.

Huettner, J.E. (1989). Indole-2-carboxylic acid: a competitive antagonist of potentiation by glycine at the NMDA receptor. Science *243*, 1611–1613.

Hui, G.K., Figueroa, I.R., Poytress, B.S., Roozendaal, B., McGaugh, J.L., and Weinberger, N.M. (2004). Memory enhancement of classical fear conditioning by post-training injections of corticosterone in rats. Neurobiol. Learn. Mem. *81*, 67–74.

Ishida, A., Mutoh, T., Ueyama, T., Bando, H., Masubuchi, S., Nakahara, D., Tsujimoto, G., and Okamura, H. (2005). Light activates the adrenal gland: timing of gene expression and glucocorticoid release. Cell Metab. *2*, 297–307.

Jonas, P., Major, G., and Sakmann, B. (1993). Quantal components of unitary EPSCs at the mossy fibre synapse on CA3 pyramidal cells of rat hippocampus. J. Physiol. *472*, 615–663.

Kalsbeek, A., and Buijs, R.M. (2002). Output pathways of the mammalian suprachiasmatic nucleus: coding circadian time by transmitter selection and specific targeting. Cell Tissue Res. *309*, 109–118.

Kasahara, T., Abe, K., Mekada, K., Yoshiki, A., and Kato, T. (2010). Genetic variation of melatonin productivity in laboratory mice under domestication. Proc. Natl. Acad. Sci. USA *107*, 6412–6417.

Kim, J.J., and Yoon, K.S. (1998). Stress: metaplastic effects in the hippocampus. Trends Neurosci. *21*, 505–509.

Kwapis, J.L., Alaghband, Y., Kramár, E.A., López, A.J., Vogel Ciernia, A., White, A.O., Shu, G., Rhee, D., Michael, C.M., Montellier, E., et al. (2018).

Epigenetic regulation of the circadian gene Per1 contributes to age-related changes in hippocampal memory. Nat. Commun. *9*, 3323.

Kwon, H.B., and Sabatini, B.L. (2011). Glutamate induces de novo growth of functional spines in developing cortex. Nature *474*, 100–104.

Lamberti, P.W., Martin, M.T., Plastino, A., and Rosso, O.A. (2004). Intensive entropic non-triviality measure. Physica A *334*, 119–131.

Lavialle, M., Aumann, G., Anlauf, E., Pröls, F., Arpin, M., and Derouiche, A. (2011). Structural plasticity of perisynaptic astrocyte processes involves ezrin and metabotropic glutamate receptors. Proc. Natl. Acad. Sci. USA *108*, 12915–12919.

Lehman, M.N., Silver, R., Gladstone, W.R., Kahn, R.M., Gibson, M., and Bittman, E.L. (1987). Circadian rhythmicity restored by neural transplant. Immunocytochemical characterization of the graft and its integration with the host brain. J. Neurosci. *7*, 1626–1638.

Lehre, K.P., and Danbolt, N.C. (1998). The number of glutamate transporter subtype molecules at glutamatergic synapses: chemical and stereological quantification in young adult rat brain. J. Neurosci. *18*, 8751–8757.

Lester, R.A.J., and Jahr, C.E. (1992). NMDA channel behavior depends on agonist affinity. J. Neurosci. *12*, 635–643.

Longair, M.H., Baker, D.A., and Armstrong, J.D. (2011). Simple Neurite Tracer: open source software for reconstruction, visualization and analysis of neuronal processes. Bioinformatics *27*, 2453–2454.

Marr, D. (1971). Simple memory: a theory for archicortex. Philos. Trans. R. Soc. Lond. B Biol. Sci. *262*, 23–81.

McEown, K., and Treit, D. (2011). Mineralocorticoid receptors in the medial prefrontal cortex and hippocampus mediate rats' unconditioned fear behaviour. Horm. Behav. *60*, 581–588.

Meijer, J.H., Watanabe, K., Schaap, J., Albus, H., and Détári, L. (1998). Light responsiveness of the suprachiasmatic nucleus: long-term multiunit and single-unit recordings in freely moving rats. J. Neurosci. *18*, 9078–9087.

Meyer-Bernstein, E.L., Jetton, A.E., Matsumoto, S.I., Markuns, J.F., Lehman, M.N., and Bittman, E.L. (1999). Effects of suprachiasmatic transplants on circadian rhythms of neuroendocrine function in golden hamsters. Endocrinology *140*, 207–218.

Migliore, M., and Shepherd, G.M. (2002). Emerging rules for the distributions of active dendritic conductances. Nat. Rev. Neurosci. *3*, 362–370.

Migliore, R., Lupascu, C.A., Bologna, L.L., Romani, A., Courcol, J.D., Antonel, S., Van Geit, W.A.H., Thomson, A.M., Mercer, A., Lange, S., et al. (2018). The physiological variability of channel density in hippocampal CA1 pyramidal cells and interneurons explored using a unified data-driven modeling workflow. PLoS Comput. Biol. *14*, e1006423.

Moore, R.Y. (1996). Neural control of the pineal gland. Behav. Brain Res. *73*, 125–130.

Moore, R.Y., and Lenn, N.J. (1972). A retinohypothalamic projection in the rat. J. Comp. Neurol. *146*, 1–14.

Musshoff, U., Riewenherm, D., Berger, E., Fauteck, J.D., and Speckmann, E.J. (2002). Melatonin receptors in rat hippocampus: molecular and functional investigations. Hippocampus *12*, 165–173.

Namihira, M., Honma, S., Abe, H., Tanahashi, Y., Ikeda, M., and Honma, K. (1999). Daily variation and light responsiveness of mammalian clock gene, Clock and BMAL1, transcripts in the pineal body and different areas of brain in rats. Neurosci. Lett. *267*, 69–72.

Nicholson, C., and Hrabětová, S. (2017). Brain extracellular space: the final frontier of neuroscience. Biophys. J. *113*, 2133–2142.

Nielsen, T.A., DiGregorio, D.A., and Silver, R.A. (2004). Modulation of glutamate mobility reveals the mechanism underlying slow-rising AMPAR EPSCs and the diffusion coefficient in the synaptic cleft. Neuron *42*, 757–771.

Nishida, H., and Okabe, S. (2007). Direct astrocytic contacts regulate local maturation of dendritic spines. J. Neurosci. *27*, 331–340.

O'Donnell, C., and van Rossum, M.C. (2014). Systematic analysis of the contributions of stochastic voltage gated channels to neuronal noise. Front. Comput. Neurosci. *8*, 105.

Ozcan, M., Yilmaz, B., and Carpenter, D.O. (2006). Effects of melatonin on synaptic transmission and long-term potentiation in two areas of mouse hippocampus. Brain Res. *1111*, 90–94.

Papouin, T., Dunphy, J.M., Tolman, M., Dineley, K.T., and Haydon, P.G. (2017). Septal cholinergic neuromodulation tunes the astrocyte-dependent gating of hippocampal NMDA receptors to wakefulness. Neuron *94*, 840–854.e847.

Pavlides, C., Watanabe, Y., Magariños, A.M., and McEwen, B.S. (1995). Opposing roles of type I and type II adrenal steroid receptors in hippocampal long-term potentiation. Neuroscience *68*, 387–394.

Peirson, S.N., Brown, L.A., Pothecary, C.A., Benson, L.A., and Fisk, A.S. (2018). Light and the laboratory mouse. J. Neurosci. Methods *300*, 26–36.

Pennington, Z.T., Dong, Z., Feng, Y., Vetere, L.M., Page-Harley, L., Shuman, T., and Cai, D.J. (2019). ezTrack: An open-source video analysis pipeline for the investigation of animal behavior. Sci. Rep. *9*, 19979.

Qi, X.R., Kamphuis, W., Wang, S., Wang, Q., Lucassen, P.J., Zhou, J.N., and Swaab, D.F. (2013). Aberrant stress hormone receptor balance in the human prefrontal cortex and hypothalamic paraventricular nucleus of depressed patients. Psychoneuroendocrinology *38*, 863–870.

Quirk, J.C., and Nisenbaum, E.S. (2002). LY404187: a novel positive allosteric modulator of AMPA receptors. CNS Drug Rev. *8*, 255–282.

Rafii-El-Idrissi, M., Calvo, J.R., Harmouch, A., García-Mauriño, S., and Guerrero, J.M. (1998). Specific binding of melatonin by purified cell nuclei from spleen and thymus of the rat. J. Neuroimmunol. *86*, 190–197.

Raghavan, A.V., Horowitz, J.M., and Fuller, C.A. (1999). Diurnal modulation of long-term potentiation in the hamster hippocampal slice. Brain Res. *833*, 311–314.

Rakic, P., Bourgeois, J.P., Eckenhoff, M.F., Zecevic, N., and Goldman-Rakic, P.S. (1986). Concurrent overproduction of synapses in diverse regions of the primate cerebral cortex. Science *232*, 232–235.

Rawashdeh, O., de Borsetti, N.H., Roman, G., and Cahill, G.M. (2007). Melatonin suppresses nighttime memory formation in zebrafish. Science *318*, 1144–1146.

Rawashdeh, O., Parsons, R., and Maronde, E. (2018). Clocking in time to gate memory processes: the circadian clock is part of the ins and outs of memory. Neural Plast. *2018*, 6238989.

Reichenbach, A., Derouiche, A., and Kirchhoff, F. (2010). Morphology and dynamics of perisynaptic glia. Brain Res. Brain Res. Rev. *63*, 11–25.

Reick, M., Garcia, J.A., Dudley, C., and McKnight, S.L. (2001). NPAS2: an analog of clock operative in the mammalian forebrain. Science *293*, 506–509.

Richards, D.A., Mateos, J.M., Hugel, S., de Paola, V., Caroni, P., Gähwiler, B.H., and McKinney, R.A. (2005). Glutamate induces the rapid formation of spine head protrusions in hippocampal slice cultures. Proc. Natl. Acad. Sci. USA *102*, 6166–6171.

Rosenfeld, P., Van Eekelen, J.A., Levine, S., and De Kloet, E.R. (1988). Ontogeny of the type 2 glucocorticoid receptor in discrete rat brain regions: an immunocytochemical study. Brain Res. *470*, 119–127.

Rosso, O.A., Larrondo, H.A., Martin, M.T., Plastino, A., and Fuentes, M.A. (2007). Distinguishing noise from chaos. Phys. Rev. Lett. *99*, 154102.

Ruby, N.F., Hwang, C.E., Wessells, C., Fernandez, F., Zhang, P., Sapolsky, R., and Heller, H.C. (2008). Hippocampal-dependent learning requires a functional circadian system. Proc. Natl. Acad. Sci. USA *105*, 15593–15598.

Salituro, F.G., Harrison, B.L., Baron, B.M., Nyce, P.L., Stewart, K.T., and McDonald, I.A. (1990). 3-(2-carboxyindol-3-yl)propionic acid derivatives: antagonists of the strychnine-insensitive glycine receptor associated with the N-methyl-D-aspartate receptor complex. J. Med. Chem. *33*, 2944–2946.

Salituro, F.G., Harrison, B.L., Baron, B.M., Nyce, P.L., Stewart, K.T., Kehne, J.H., White, H.S., and McDonald, I.A. (1992). 3-(2-Carboxyindol-3-yl)propionic acid-based antagonists of the N-methyl-D-aspartic acid receptor associated glycine binding site. J. Med. Chem. *35*, 1791–1799.

Saunders, A., Macosko, E.Z., Wysoker, A., Goldman, M., Krienen, F.M., de Rivera, H., Bien, E., Baum, M., Bortolin, L., Wang, S., et al. (2018). Molecular

diversity and specializations among the cells of the adult mouse brain. Cell *174*, 1015–1030.e16.

Scimemi, A., and Diamond, J.S. (2013). Deriving the time course of glutamate clearance with a deconvolution analysis of astrocytic transporter currents. J. Vis. Exp. (*78*), 50708.

Scimemi, A., Fine, A., Kullmann, D.M., and Rusakov, D.A. (2004). NR2B-containing receptors mediate cross talk among hippocampal synapses. J. Neurosci. *24*, 4767–4777.

Scimemi, A., Semyanov, A., Sperk, G., Kullmann, D.M., and Walker, M.C. (2005). Multiple and plastic receptors mediate tonic GABAA receptor currents in the hippocampus. J. Neurosci. *25*, 10016–10024.

Scimemi, A., Tian, H., and Diamond, J.S. (2009). Neuronal transporters regulate glutamate clearance, NMDA receptor activation, and synaptic plasticity in the hippocampus. J. Neurosci. *29*, 14581–14595.

Scimemi, A., Meabon, J.S., Woltjer, R.L., Sullivan, J.M., Diamond, J.S., and Cook, D.G. (2013). Amyloid-β1-42 slows clearance of synaptically released glutamate by mislocalizing astrocytic GLT-1. J. Neurosci. *33*, 5312–5318.

Semyanov, A., Walker, M.C., and Kullmann, D.M. (2003). GABA uptake regulates cortical excitability via cell type-specific tonic inhibition. Nat. Neurosci. *6*, 484–490.

Semyanov, A., Walker, M.C., Kullmann, D.M., and Silver, R.A. (2004). Tonically active GABA A receptors: modulating gain and maintaining the tone. Trends Neurosci. *27*, 262–269.

Shimizu, K., Kobayashi, Y., Nakatsuji, E., Yamazaki, M., Shimba, S., Sakimura, K., and Fukada, Y. (2016). SCOP/PHLPP1β mediates circadian regulation of long-term recognition memory. Nat. Commun. *7*, 12926.

Shiromani, P.J., Xu, M., Winston, E.M., Shiromani, S.N., Gerashchenko, D., and Weaver, D.R. (2004). Sleep rhythmicity and homeostasis in mice with targeted disruption of mPeriod genes. Am. J. Physiol. Regul. Integr. Comp. Physiol. *287*, R47–R57.

Smarr, B.L., Jennings, K.J., Driscoll, J.R., and Kriegsfeld, L.J. (2014). A time to remember: the role of circadian clocks in learning and memory. Behav. Neurosci. *128*, 283–303.

Snider, K.H., Dziema, H., Aten, S., Loeser, J., Norona, F.E., Hoyt, K., and Obrietan, K. (2016). Modulation of learning and memory by the targeted deletion of the circadian clock gene Bmal1 in forebrain circuits. Behav. Brain Res. *308*, 222–235.

Sousa, A.A., Azari, A.A., Zhang, G., and Leapman, R.D. (2011). Dual-axis electron tomography of biological specimens: Extending the limits of specimen thickness with bright-field STEM imaging. J. Struct. Biol. *174*, 107–114.

Stell, B.M., Brickley, S.G., Tang, C.Y., Farrant, M., and Mody, I. (2003). Neuroactive steroids reduce neuronal excitability by selectively enhancing tonic inhibition mediated by delta subunit-containing GABAA receptors. Proc. Natl. Acad. Sci. USA *100*, 14439–14444.

Stephan, F.K., and Zucker, I. (1972). Circadian rhythms in drinking behavior and locomotor activity of rats are eliminated by hypothalamic lesions. Proc. Natl. Acad. Sci. USA *69*, 1583–1586.

Sumová, A., Bendová, Z., Sládek, M., El-Hennamy, R., Matejů, K., Polidarová, L., Sosniyenko, S., and Illnerová, H. (2008). Circadian molecular clocks tick along ontogenesis. Physiol. Res. *57* (*Suppl 3*), S139–S148.

Sumova, A., Sladek, M., Polidarova, L., Novakova, M., and Houdek, P. (2012). Circadian system from conception till adulthood. Prog. Brain Res. *199*, 83–103.

Sweeney, A.M., Fleming, K.E., McCauley, J.P., Rodriguez, M.F., Martin, E.T., Sousa, A.A., Leapman, R.D., and Scimemi, A. (2017). PAR1 activation induces rapid changes in glutamate uptake and astrocyte morphology. Sci. Rep. *7*, 43606.

Thomas-Crusells, J., Vieira, A., Saarma, M., and Rivera, C. (2003). A novel method for monitoring surface membrane trafficking on hippocampal acute slice preparation. J. Neurosci. Methods *125*, 159–166.

Tillberg, P.W., Chen, F., Piatkevich, K.D., Zhao, Y., Yu, C.C., English, B.P., Gao, L., Martorell, A., Suk, H.J., Yoshida, F., et al. (2016). Protein-retention expansion microscopy of cells and tissues labeled using standard fluorescent proteins and antibodies. Nat. Biotechnol. *34*, 987–992.

Tsodyks, M., Pawelzik, K., and Markram, H. (1998). Neural networks with dynamic synapses. Neural Comput. *10*, 821–835.

Vanecek, J. (1998). Cellular mechanisms of melatonin action. Physiol. Rev. *78*, 687–721.

Venkova, K., Foreman, R.D., and Greenwood-Van Meerveld, B. (2009). Mineralocorticoid and glucocorticoid receptors in the amygdala regulate distinct responses to colorectal distension. Neuropharmacology *56*, 514–521.

Wakamatsu, H., Yoshinobu, Y., Aida, R., Moriya, T., Akiyama, M., and Shibata, S. (2001). Restricted-feeding-induced anticipatory activity rhythm is associated with a phase-shift of the expression of mPer1 and mPer2 mRNA in the cerebral cortex and hippocampus but not in the suprachiasmatic nucleus of mice. Eur. J. Neurosci. *13*, 1190–1196.

Wang, L.M., Suthana, N.A., Chaudhury, D., Weaver, D.R., and Colwell, C.S. (2005). Melatonin inhibits hippocampal long-term potentiation. Eur. J. Neurosci. *22*, 2231–2237.

Wang, L.M., Dragich, J.M., Kudo, T., Odom, I.H., Welsh, D.K., O'Dell, T.J., and Colwell, C.S. (2009). Expression of the circadian clock gene Period2 in the hippocampus: possible implications for synaptic plasticity and learned behaviour. ASN Neuro *1*, e00012.

Weickert, J., and Scharr, H. (2002). A scheme for coherence-enhancing diffusion filtering with optimized rotation invariance. J Vis Commun Image R *13*, 103–118.

Weinert, D. (2005). Ontogenetic development of the mammalian circadian system. Chronobiol. Int. *22*, 179–205.

Whitehead, G., Jo, J., Hogg, E.L., Piers, T., Kim, D.H., Seaton, G., Seok, H., Bru-Mercier, G., Son, G.H., Regan, P., et al. (2013). Acute stress causes rapid synaptic insertion of Ca2+ -permeable AMPA receptors to facilitate long-term potentiation in the hippocampus. Brain *136*, 3753–3765.

Willshaw, D.J., Dayan, P., and Morris, R.G. (2015). Memory, modelling and Marr: a commentary on Marr (1971) 'Simple memory: a theory of archicortex'. Philos. Trans. R. Soc. Lond. B Biol. Sci. *370*, 20140383.

Winson, J., and Abzug, C. (1977). Gating of neuronal transmission in the hippocampus: efficacy of transmission varies with behavioral state. Science *196*, 1223–1225.

Winson, J., and Abzug, C. (1978). Neuronal transmission through hippocampal pathways dependent on behavior. J. Neurophysiol. *41*, 716–732.

Yuen, E.Y., Liu, W., Karatsoreos, I.N., Ren, Y., Feng, J., McEwen, B.S., and Yan, Z. (2011). Mechanisms for acute stress-induced enhancement of glutamatergic transmission and working memory. Mol. Psychiatry *16*, 156–170.

Zheng, B., Albrecht, U., Kaasik, K., Sage, M., Lu, W., Vaishnav, S., Li, Q., Sun, Z.S., Eichele, G., Bradley, A., and Lee, C.C. (2001). Nonredundant roles of the mPer1 and mPer2 genes in the mammalian circadian clock. Cell *105*, 683–694.

Zheng, C., Bieri, K.W., Hwaun, E., and Colgin, L.L. (2016). Fast gamma rhythms in the hippocampus promote encoding of novel object-place pairings. eNeuro *3*, ENEURO.0001-16.2016.

STAR★METHODS

KEY RESOURCES TABLE

REAGENT or RESOURCE	SOURCE	IDENTIFIER
Antibodies		
Rabbit anti GLAST	Cell Signaling Technology	Cell Signaling Technologies: 5684; RRID: AB_10695722
Rabbit anti GLT-1	Cell Signaling Technology	Cell Signaling Technologies: 3838; RRID: AB_2190743
Rabbit anti b-actin	Cell Signaling Technology	Cell Signaling Technologies: 4970; RRID: AB_2223172
Biotinylated horse anti-rabbit	Vector Laboratories	Vector Laboratories: BA-1100; RRID: AB_2336201
Chemicals, Peptides, and Recombinant Proteins		
Tetrodotoxin (TTX)	Hello Bio	Hello Bio: HB1035
2,3-Dioxo-6-nitro-1,2,3,4-tetrahydrobenzo[f]quinoxaline-7-sulfonamide disodium salt (NBQX)	Hello Bio	Hello Bio: HB0443
D,L-2-Amino-5-phosphonopentanoic acid (APV)	Hello Bio	Hello Bio: HB0251
3S)-3-[[3-[[4-(Trifluoromethyl)benzoyl]amino]phenyl] methoxy]-L-aspartic acid (TFB-TBOA)	Tocris	Tocris: 2532
Spironolactone	Cayman Chemical Company	Cayman Chemical Company: 9000324
Mifepristone	Cayman Chemical Company	Cayman Chemical Company: 10006317
Luzindole	Cayman Chemical Company	Cayman Chemical Company: 15598
Fluoromount G	SouthernBiotech	SouthernBiotech: 0100-01
DAPI Fluoromount G	SouthernBiotech	SouthernBiotech: 0100-02
Acryloyl X, SE	Life Technologies	Life Technologies: A20770
DMSO	Millipore Sigma	Millipore Sigma: 472301
PBS	Millipore Sigma	Millipore Sigma: P4417
Sodium acrylate	Millipore Sigma	Millipore Sigma: 408220
Acrylamide	Millipore Sigma	Millipore Sigma: A9099
N,N′-methylenebisacrylamide	Millipore Sigma	Millipore Sigma: M7279
Sodium chloride	BeanTwon Chemical	BeanTwon Chemical: 215700
4-hydroxy-TEMPO	Millipore Sigma	Millipore Sigma: 176141
TEMED	Millipore Sigma	Millipore Sigma: T9281
APS	Millipore Sigma	Millipore Sigma: A3678
Tris pH 8.0	Ambion	Ambion: AM9855G
EDTA	Fluka Analytical	Fluka Analytical: 03690
Triton X-100	Millipore Sigma	Millipore Sigma: X100
Guanidine hydrochloride	Millipore Sigma	Millipore Sigma: G3272
Proteinase K	Millipore Sigma	Millipore Sigma: P6556
sulfo-NHS-SS-biotin	VWR	VWR: PI21328
L-lysine	Millipore Sigma	Millipore Sigma: L5501
Immobilon-P PVDF membrane	Millipore Sigma	Millipore Sigma: P2563
Bipolar stainless steel electrode	Frederick Haer Corporation	Frederick Haer Corporation: MX21AES(JD3)
Critical Commercial Assays		
Vectastain Elite ABC-peroxidase kit	Vector Laboratories	Vector Laboratories: PK-6100; RRID: AB_2336819
KAPA HiFi Hot Start Ready Mix PCR Kit	Roche	Roche: KK2602
Corticosterone double antibody RIA kit	MP Biomedicals	MP Biomedicals: 07120102
Mem-PER Plus Membrane Protein Extraction Kit	ThermoFisher Scientific	ThermoFisher Scientific: 89842

(*Continued on next page*)

Continued

REAGENT or RESOURCE	SOURCE	IDENTIFIER
Deposited Data		
Raw and analyzed data	This paper	https://osf.io/k9w68/?view_only=62d2c8eb6a5c40e3896d6ef7c74131f2
Experimental Models: Organisms/Strains		
M. musculus C57BL/6NCrl	Charles River Laboratories	Charles River: 027
M. musculus $Per1^{Brdm1/Brdm1}$: $Per2^{Brdm1/Brdm1}$ (referred to as $Per1,2^{-/-}$)	Jennifer Hurley (Rensselaer Polytechnic Institute)	N/A
Oligonucleotides		
$Per1^{+/+}$ Forward: 5′ CAA-ACT-CAC-AGA-GCC-CAT-C 3′	Eurofins Genomics	N/A
$Per1^{+/+}$ Reverse: 5′ CAT-GAG-TTC-TTT-CTG-GGT-CC 3′	Eurofins Genomics	N/A
$Per1^{-/-}$ Forward: 5′ CAA-ACT-CAC-AGA-GCC-CAT-C 3′	Eurofins Genomics	N/A
$Per1^{-/-}$ Reverse: 5′ CTT-TTG-AAG-CGT-GCA-GAA-TG 3′	Eurofins Genomics	N/A
$Per2^{+/+}$ Forward: 5′ TTC-CAC-TCT-GTG-GGT-TTT-GG 3′	Eurofins Genomics	N/A
$Per2^{+/+}$ Reverse: 5′ AAA-GGG-CCT-CTG-TGT-GAT-TG 3′	Eurofins Genomics	N/A
$Per2^{-/-}$ Forward: 5′ TTC-CAC-TCT-GTG-GGT-TTT-GG 3′	Eurofins Genomics	N/A
$Per2^{-/-}$ Reverse: 5′ GCC-AGA-GGC-CAC-TTG-TGT-AG 3′	Eurofins Genomics	N/A
Software and Algorithms		
IgorPro 6.37	Wavemetrics	N/A
Jupyter Notebook	Project Jupyter	N/A
Blender 2.79	Blender Corporation	N/A
CellBlender 1.1	MCell	N/A
NEURON	Yale University	N/A
Fiji	ImageJ	N/A
ezTrack	Denise Cai (Mount Sinai)	N/A
IMOD 4.7	David Mastronarde (University of Colorado)	N/A
Blender 2.76	Blender Corporation	N/A
STEVE	Nanolive	N/A
Simple Neurite Tracer 3.1.3	Tiago Ferreira (HHMI - Janelia Research Campus)	N/A
Other		
RNAscope probe for Per2	Advanced Cell Diagnostics	Advanced Cell Diagnostics: Mm-Per2-C1
RNAscope probe for Arntl	Advanced Cell Diagnostics	Advanced Cell Diagnostics: Mm-Arntl-C2
Opal reactive fluorophore (green)	Akoya Biosciences	Akoya Biosciences: Opal 520
Opal reactive fluorophore (red)	Akoya Biosciences	Akoya Biosciences: Opal 570

RESOURCE AVAILABILITY

Lead Contact

Further information and requests for resources and reagents should be directed to the Lead Contact, Annalisa Scimemi (scimemia@gmail.com or ascimemi@albany.edu).

Materials Availability

This study did not generate new unique reagents.

Data and Code Availability

Original data and analyzed data have been deposited to Open Science Framework (https://osf.io/k9w68/?view_only=62d2c8eb6a5c40e3896d6ef7c74131f2). All data, custom scripts and functions used for this study are available from the lead contact scimemia@gmail.com upon request.

EXPERIMENTAL MODEL AND SUBJECT DETAILS

All experimental procedures were performed in accordance with protocols approved by the Institutional Animal Care and Use Committee at the State University of New York (SUNY) Albany and guidelines described in the National Institutes of Health's Guide for the Care and Use of Laboratory Animals. Unless otherwise stated, all mice were group housed and kept under 12 h:12 h L/D conditions (lights on at 7 AM, ZT0; lights off at 7 PM, ZT12). We refer to the ZT0-12 time interval as the L phase, and the ZT12-24 time interval as the D phase. The ZT time sets the origin of the 24 hour period to the beginning of the L phase, facilitating cross-study comparisons independently of the actual clock-time settings of different animal facilities.

C57BL/6NCrl line

We used mice from the C57BL/6NCrl line of either sex. A subset of experiments were performed using mice kept under constant darkness (i.e., 12 h:12 h D/D conditions under red dim light illumination for at least three cycles). The dim red light intensity in constant darkness matched that of the D phase for mice kept under 12 h:12 h L/D conditions. For mice maintained in constant darkness, the ZT0-12 time interval was referred to as the subjective L phase, and the ZT12-24 time interval as the subjective D phase. Food and water were available *ad libitum* to all mice throughout the 24 hour period. Unless otherwise stated, all dissections for the data collected in the L and subjective L phase were performed at ZT3.5. All dissections for the D and subjective D phase data were performed at ZT15.5.

Per1/2$^{-/-}$ line

We used mice with targeted disruption of *Per1* and *Per2* alleles (Per1$^{Brdm1/Brdm1}$: Per2$^{Brdm1/Brdm1}$), here referred to as Per1/2$^{-/-}$ mice, of either sex. These mice were a generous gift from Dr. Jennifer Hurley (RPI) and have been characterized in previous works (Bae et al., 2001; Shiromani et al., 2004; Zheng et al., 2001). A subset of experiments were performed using mice kept under constant darkness (i.e., 12 h:12 h D/D conditions under red dim light illumination for at least three cycles). The dim red light intensity in constant darkness matched that of the D phase for mice kept under 12 h:12 h L/D conditions. Food and water were available *ad libitum* to all mice throughout the 24 hour period. Unless otherwise stated, all dissections for the data collected in the L and subjective L phase were performed at ZT3.5. All dissections for the D and subjective D phase data were performed at ZT15.5.

METHOD DETAILS

Genotyping

Genotyping was performed on toe tissue samples of P7–P10 mice. Briefly, tissue samples were digested at 55°C overnight with shaking at 330 rpm in a lysis buffer containing the following (in mM): 100 Tris base, pH 8, 5 EDTA, and 200 NaCl, along with 0.2% SDS and 50 μg/ml proteinase K. Following heat inactivation of Proteinase K at 97°C for 10 min, DNA samples were diluted 1:1 with nuclease-free water. The PCR primers used for Per1 and Per2 were purchased from Eurofins Genomics and their nucleotide sequences are listed in the table below.

Gene	Forward primer	Reverse primer	Band size (bp)
Per1$^{+/+}$	5′ CAA-ACT-CAC-AGA-GCC-CAT-C 3′	5′ CAT-GAG-TTC-TTT-CTG-GGT-CC 3′	234
Per1$^{-/-}$	5′ CAA-ACT-CAC-AGA-GCC-CAT-C 3′	5′ CTT-TTG-AAG-CGT-GCA-GAA-TG 3′	700
Per2$^{+/+}$	5′ TTC-CAC-TCT-GTG-GGT-TTT-GG 3′	5′ AAA-GGG-CCT-CTG-TGT-GAT-TG 3′	297
Per2$^{-/-}$	5′ TTC-CAC-TCT-GTG-GGT-TTT-GG 3′	5′ GCC-AGA-GGC-CAC-TTG-TGT-AG 3′	200

The forward and reverse primers for *Per1* are located in exons 3 and 4, respectively. The reverse primer for *Per1*$^{-/-}$ mice is located in the mPGK promoter for the *Hprt* cassette that replaces exons 4 through 18 of *Per1*$^{-/-}$ mice. The forward and reverse primers for *Per2* are located within intron 11-12. The reverse primer for *Per2*$^{-/-}$ mice is located in the Neomycin cassette that replaces the highly conserved PAS domain in *Per2*$^{-/-}$ mice. PCR was carried out using the KAPA HiFi Hot Start Ready Mix PCR Kit (KAPA Biosystems, KK2602). Briefly, 12.5 μl of 2X KAPA HiFi Hot Start Ready Mix was added to 11.5 μl of a diluted primer mix (0.5-0.75 μM final concentration for each primer) and 1 μl of diluted DNA. The PCR cycling protocols for *Per1* and *Per2* are described in the tables below.

Per1	Initiation/melting	Denaturation	Annealing	Elongation	Amplification	Hold
Temperature (°C)	95	95	60	72	72	4
Duration (min)	3	0.25	0.25	0.5	1	∞
Cycles	1	35			1	

Per2	Initiation/melting	Denaturation	Annealing	Elongation	Amplification	Hold
Temperature (°C)	95	95	56	72	72	4
Duration (min)	3	0.25	0.25	0.25	1	∞
Cycles	1	35			1	

In vivo chronic temperature recordings

To record the mouse body temperature, we implanted programmable micro-transponders (Cat# IPTT300; BDMS) under the skin of the neck of P12 mice. We took temperature measures hourly from P14–21 using a wireless hand-held reader for IPTT micro-transponders (Cat# DAS-8007-IUS, BDMS). Data analysis was performed in IgorPro 6.37 (Wavemetrics, Lake Oswego, OR) using custom-made software (A. Scimemi).

Fluorescent *in situ* hybridization of clock gene transcripts using RNAscope fluorescence *in situ* hybridization (FISH)

We dissected the brain of P14-21 C57BL/6NCrl mice at ZT3.5 or ZT15.5, removed the olfactory bulbs, cerebellum and temporal lobes and fixed it with 4% PFA/PBS overnight at 4°C. The brain was then cryo-protected in 30% sucrose PBS at 4°C for 48 hour and stored in PBS for no more than a week. To prepare slices for RNAscope, we separated the two hemispheres, embedded them in agar and prepared 40 μm thick slices using a vibrating blade microtome (VT1200S, Leica Microsystems, Buffalo Grove, IL). The slices were post-fixed in 4% PFA/PBS for 30 min at room temperature (RT) and mounted onto Superfrost plus microscope slides. Mounted slices were used for fluorescence *in situ* hybridization (FISH) using an RNAscope multiplex fluorescent assay (Advanced Cell Diagnostics, Newark, CA) according to manufacturer instructions, using Mm-Per2-C1 and Mm-Arntl-C2 RNA probes and Opal 520 and Opal 570 dyes (Akoya Biosciences, Menlo Park, CA). DAPI Fluoromount G was used as the mounting medium (Cat# 0100-02; SouthernBiotech, Birmingham, AL). The presence of *Per2* and *Arntl* transcripts was assessed using a confocal microscope (Zeiss LSM710) equipped with a Plan-Apochromat 63X/1.4NA oil objective. Image size was set to 1024x1024 pixels and represented the average of 8 consecutive frames.

Acute slice preparation and electrophysiology recordings

Acute coronal slices of the mouse hippocampus were obtained from C57BL/6NCrl mice of either sex (P14–21), deeply anesthetized with isoflurane and decapitated in accordance with SUNY Albany Animal Care and Use Committee guidelines. The brain was rapidly removed and placed in ice-cold slicing solution bubbled with 95% O_2/5% CO_2 containing the following (in mM): 119 NaCl, 2.5 KCl, 0.5 $CaCl_2$, 1.3 $MgSO_4 \cdot H_2O$, 4 $MgCl_2$, 26.2 $NaHCO_3$, 1 NaH_2PO_4, and 22 glucose, 320 mOsm, pH 7.4. The slices (250 μm thick) were prepared using a vibrating blade microtome (VT1200S; Leica Microsystems, Buffalo Grove, IL). Once prepared, the slices were stored in slicing solution in a submersion chamber at 36°C for 30 min and at RT for at least 30 min and up to 5 hours. Unless otherwise stated, the recording solution contained the following (in mM): 119 NaCl, 2.5 KCl, 2.5 $CaCl_2$, 1 $MgCl_2$, 26.2 $NaHCO_3$, and 1 NaH_2PO_4, 22 glucose, 300 mOsm, pH 7.4. We identified the hippocampus under bright field illumination using an upright fixed-stage microscope (BX51 WI; Olympus Corporation, Center Valley, PA). To record evoked currents, we delivered constant voltage stimuli (50–100 μs) to a bipolar stainless steel electrode (Cat# MX21AES(JD3); Frederick Haer Corporation, Bowdoin, ME) positioned in *s.r.*, ~100 μm away from the recorded cell. Whole-cell, voltage-clamp patch-clamp recordings were made using patch pipettes containing (in mM): 120 $CsCH_3SO_3$, 10 EGTA, 20 HEPES, 2 MgATP, 0.2 NaGTP, 5 QX-314Br, 290 mOsm, pH 7.2. All recordings were obtained using a Multiclamp 700B amplifier (Molecular Devices, San Jose, CA) and filtered at 10 KHz, converted with an 18-bit 200 kHz A/D board (HEKA Instrument, Holliston, MA), digitized at 10 KHz, and analyzed offline with custom-made software (A. Scimemi) written in IgorPro 6.37 (Wavemetrics, Lake Oswego, OR). Patch electrodes (#0010 glass; Harvard Apparatus, Holliston, MA) had tip resistances of ~5 MΩ. Series resistance (~20 MΩ) was not compensated, but was continuously monitored and experiments were discarded if this changed by > 20%. The series resistance was subtracted from the total resistance to estimate the cell membrane resistance of neurons and astrocytes. Extracellular recordings were performed using electrodes with a tip resistance of 2-5 MΩ, filled with the recording solution described above. The electrode resistance was continuously monitored and experiments were discarded if this changed by > 20%. Slices were incubated with NR3C1/2 receptor antagonists for 30 min −2 hour before being used for electrophysiology recordings. Tetrodotoxin (TTX), 2,3-Dioxo-6-nitro-1,2,3,4-tetrahydrobenzo[f]quinoxaline-7-sulfonamide disodium salt (NBQX) and D,L-2-Amino-5-phosphonopentanoic acid (APV) were purchased from Hello Bio (Princeton, NJ; Cat# HB1035, HB0443, HB0251, respectively). (3S)-3-[[3-[[4-(Trifluoromethyl)benzoyl]amino]phenyl]methoxy]-L-aspartic acid (TFB-TBOA) was purchased from Tocris (Minneapolis, MN; Cat# 2532). Spironolactone, mifepristone and luzindole were purchased from Cayman Chemical Company (Ann Arbor, MI; Cat# 9000324, 10006317, 15598, respectively). All other chemicals were purchased from MilliporeSigma (Burlington, MA). All recordings were performed at RT.

Blood collection and corticosterone radioimmunoassay

Trunk blood was collected from 18 mice kept under 12 h:12 h L/D conditions, and 18 mice kept under 12 h:12 h D/D conditions. Trunk blood was collected within 3 min of cage disturbance from 3 mice every 4 hours. Blood was centrifuged at 5500 RCF for 10 min, and supernatant was transferred to a new tube and stored at −80°C until used for radioimmunoassay for corticosterone. Plasma

corticosterone was assessed using a commercial I-125 corticosterone radioimmunoassay kit according to the manufacturer's instructions (Cat# 07120102, MP Biochemicals, LLC, Orangeburg, NY, USA). The intra-assay coefficient of variation was 3.4%. This assay kit shows a slight cross-reaction with desoxycorticosterone 0.34%, testosterone 0.10%, cortisol 0.05%, aldosterone 0.03%, and progesterone 0.02%.

Biocytin filling and confocal imaging

Biocytin 0.2%–0.4% (w/v) was added to the intracellular solution used to patch astrocytes and neurons. Each cell was patched and filled for at least 20 min. The slices were then fixed overnight at 4°C in 4% PFA/PBS, cryo-protected in 30% sucrose PBS, and incubated in 0.1% streptavidin-Alexa Fluor 488 conjugate and 0.1% Triton X-100 for 3 hour at RT. The slices were then mounted onto microscope slides using Fluoromount-G mounting medium (Cat# 0100-01; SouthernBiotech, Birmingham, AL). Confocal images were acquired using a Zeiss LSM710 inverted microscope equipped with 488 nm Ar laser. All images were acquired as z stacks using a 40X/1.4 NA oil-immersion objective. To visualize full cells, we stitched together z stacks (1024x1024 pixels) collected by averaging four frames for each focal plane (1 μm z-step). The image analysis to measure the astrocyte coverage area was performed using Fiji (https://fiji.sc/). Briefly, we generated a maximum intensity projection of each image stack and manually traced the contour of the outer boundaries of the area of the neuropil covered by each astrocyte. Confocal images that contained more than one filled astrocyte were discarded from the analysis, because they introduced inaccuracies in the derived contours. The polar plots were obtained by centering the soma of each astrocyte at the center of a polar plot. The main primary branch of each astrocyte was oriented along the 270° angle. Average coverage traces were obtained using IgorPro (Wavemetrics, Lake Oswego, OR).

Protein-retention expansion microscopy and two-photon imaging

All experiments were performed according to the proExM protocol described by (Tillberg et al., 2016). Briefly, to measure the expansion factor (Figure S5) we fixed hippocampal slices with 4% PFA/PBS overnight at 4°C, cryoprotected them in 30% sucrose PBS and stored them in PBS. The day before starting the proExM protocol, we incubated them with DAPI Fluoromount G overnight at 4°C (Cat# 0100-20; SouthernBiotech, Birmingham, AL). Slices containing biocytin filled astrocytes were fixed, cryo-protected, stored in PBS and labeled with streptavidin-Alexa Fluor 488 as described in the previous section. In both cases, each slice was then incubated with 200 μl of anchoring solution overnight at RT. The following day, the slices were gelled and digested with Proteinase K overnight at RT. Subsequently, they were expanded using three consecutive incubations with distilled water for 15 min each. Slices stained with DAPI were imaged as they expanded during each incubation period, using a 2X/0.06 NA air objective on an EVOS FL Cell Imaging System equipped with DAPI filter set (λ_{ex}: 357/44 nm, λ_{em}: 447/60 nm; ThermoFisher Scientific, Waltham, MA). Images were collected at 0.1 fps and manually traced to measure slice perimeter and surface area using IMOD (https://bio3d.colorado.edu/imod/). The expanded gels containing biocytin-filled astrocytes were then covered with 2% agarose and submerged in distilled water before being imaged with a custom-made two-photon laser-scanning microscope. The two-photon laser scanning system (Scientifica, Clarksburg, NJ) was powered by a Ti:sapphire pulsed laser (Coherent, Santa Clara, CA) tuned to 760 nm and connected to an upright microscope with a 60X/1.0 NA objective (Olympus Corporation, Center Valley, PA). The green fluorescent signal was separated from the red using a 565 nm dichroic mirror and filtered using FITC filter sets (Olympus Corporation, Center Valley, PA). We averaged eight frames for each optical section (512 × 512 pixels) and collected z stacks for a total distance of ~200 μm (in 1.2 μm steps). The composition of the anchoring, gelling and digestion solution is reported in the table below.

Anchoring solution (200 μl/slice)	Cat#	Supplier	Amount
Acryloyl X, SE	A20770	Life Technologies	0.1 mg/ml
DMSO	472301	Millipore Sigma	2 μl
PBS	P4417	Millipore Sigma	198 μl

Monomer solution (188 μl/slice)	Cat#	Supplier	Amount
Sodium acrylate	408220	Millipore Sigma	86 mg/ml
Acrylamide	A9099	Millipore Sigma	25 mg/ml
N,N′-methylenebisacrylamide	M7279	Millipore Sigma	1.5 mg/ml
NaCl	215700	BeanTwon Chemical	117 mg/ml
PBS 10X	P4417	Millipore Sigma	18.8 μl (1:10)
Distilled water			169.2 μl

Gelling solution (200 μl/slice)	Cat#	Supplier	Amount
Monomer solution			188 μl
4-hydroxy-TEMPO	176141	Millipore Sigma	4 μl (0.01%)
TEMED	T9281	Millipore Sigma	4 μl (0.2% w/w)
APS	A3678	Millipore Sigma	4 μl (0.2% w/w)

Digestion solution (200 μl/slice)	Cat#	Supplier	Amount
Tris pH 8.0	AM9855G	Ambion	50 mM
EDTA	03690	Fluka Analytical	1 mM
Triton X-100	X100	Millipore Sigma	0.5% v/v
Guanidine hydrochloride	G3272	Millipore Sigma	0.8 M
Proteinase K	P6556	Millipore Sigma	8 U/ml

Western blot

Western blot experiments were performed on protein extracts from the hippocampus of mice of either sex aged P14–21, sacrificed at ZT3.5 or ZT15.5. Membrane proteins were extracted using the Mem-PER Plus Membrane Protein Extraction Kit (Cat# 89842; ThermoFisher Scientific, Waltham, MA) according to the manufacturer's instructions using a mixture of protease and phosphatase inhibitors (10 μl/ml, Cat# 78441; ThermoFisher Scientific, Waltham, MA). The total membrane protein concentration was determined by spectrophotometry. Equal amounts of protein (100 μg) from each sample were resolved on 10 or 12% acrylamide gels. The proteins were transferred to PVDF membranes (Cat# P2563; MilliporeSigma, Burlington, MA) using a semidry blotting approach. The membranes were blocked with 5% nonfat milk in TBST pH 7.6, and probed with primary antibodies overnight at 4°C in 5% BSA in TBST, pH 7.6. Secondary antibody incubation was performed for 1–2 hour at RT in 5% nonfat milk in TBST, pH 7.6. Pre-adsorption experiments were performed using the control antigen provided by the primary antibody supplier according to the manufacturer's instructions (1 μg/μg antibody). Membranes were probed with either rabbit anti-GLAST (1:1,000), anti-GLT1 (1:1,000) or β-actin antibodies (1:1,000). Biotinylated horse anti-rabbit antibody was used as the secondary antibody for all blots (1:1,000 for GLAST and GLT1, 1:5,000 for β-actin). We amplified the immuno-labeling reactions using the Vectastain ABC kit (1:2,000 for GLAST and GLT1; 1:5,000 for β-actin) and the Clarity Western ECL system served as the substrate for the peroxidase enzyme (Cat# 1705060, Bio-Rad, Hercules, CA). For semiquantitative analysis, protein band intensities were collected as 16-bit images using a digital chemiluminescence imaging system (c300, Azure Biosystems, Dublin, CA) at different exposure times (0.5–200 s). Each image was converted to an 8-bit image for image analysis using Fiji software (https://fiji.sc/). Only images collected at exposure times that did not lead to pixel saturation were included in the analysis. The intensity of each band was calculated as the mean gray value in a region of interest (ROI) surrounding each band in three images collected at different exposure times. All GLAST and GLT1 band intensities were normalized to the band intensity of β-actin in the same lane. Only images collected at exposure times that did not lead to pixel saturation were used to quantify band intensities. A list of antibodies and reagents, with their RRID, is reported in the table below and in the Key Resources Table.

RRID	Item	Supplier
AB_10695722	rabbit anti GLAST	Cell Signaling Technology, Danvers, MA
AB_2190743	rabbit anti GLT1	Cell Signaling Technology, Danvers, MA
AB_2223172	rabbit anti β-actin	Cell Signaling Technology, Danvers, MA
AB_2336201	biotinylated horse anti-rabbit	Vector Laboratories, Burlingame, CA
AB_2336819	Vectastain ABC kit	Vector Laboratories, Burlingame, CA

Surface protein biotinylation assay

We prepared acute hippocampal slices following the same experimental procedures used to prepare acute slices for electrophysiology recordings. Once prepared, the slices were stored in slicing solution in a submersion chamber at 36°C for 30 min and at RT for at least 30 min and up to 1 hour. Subsequently, the slices were processed following the biotinylation protocol developed and validated by (Thomas-Crusells et al., 2003). *First,* the acute hippocampal slices were washed twice for 5 min in ice-cold slicing solution,

here referred to as modified artificial cerebrospinal fluid (mACSF), and then transferred to a 24-well plate containing mACSF added with 100 μM sulfo-NHS-SS-biotin (Cat# PI21328, VWR, Radnor, PA) for 45 min, on ice. The slices were then washed twice with cold mACSF containing 1 mM L-lysine (Cat# L5501, Millipore Sigma, Burlington, MA), to block all excess reactive sulfo-NHS-SS-biotin. We dissected the hippocampus out of the biotinylated slices, pooled the slices in an Eppendorf tube and removed the excess supernatant. The membrane proteins were isolated according to the Mem-Per Plus Membrane Protein Extraction Kit (Cat#89842, ThermoFisher Scientific, Waltham, MA). Subsequently, the membrane protein fraction was incubated with 40 μl of Ultra-link immobilized Streptavidin beads (Pierce Streptavidin UltraLink Resin, Cat# 53113, ThermoFisher Scientific, Waltham, MA) with gentle rotation overnight at 4°C. The following day, the beads were washed three times (5,000 × g at 4°C for 2 min) in solubilization buffer containing protease inhibitors and biotinylated proteins were released from the beads with 40 μl of solubilization buffer containing 5% β-mercaptoethanol and stored at −20°C until further use. The biotinylated proteins were separated by 10% SDS-PAGE and transferred to an Immobilon-P PVDF membrane (Cat# P2563, Millipore Sigma, Burlington, MA). The membranes were blocked at RT for 1 hour with 5% BSA (Cat# A9418, Millipore Sigma, Burlington, MA) in Tris Buffered Saline, pH 7.5, containing 0.1% Tween-20 (TBS-T), and immunoblotted overnight at 4°C with rabbit anti-GLAST (1:1,000), GLT1 (1:1,000) or β-actin (1:5,000) (Cat# listed above, Cell Signaling Technology, Danvers, MA) in 5% BSA/TBS-T. The secondary antibody, biotinylated horse anti-rabbit (Vector Laboratories, Burlingame, CA) was incubated for 1 h at RT in 5% BSA/TBS-T (1:1,000 for GLAST and GLT1; 1:5,000 for β-actin). Immuno-labeling reactions were amplified using the Vectastain ABC kit (1:2,000 for GLAST and GLT1; 1:5,000 for β-actin) and the Clarity Western ECL system served as the substrate for the peroxidase enzyme (Cat# 1705060, Bio-Rad, Hercules, CA). For semiquantitative analysis, protein band intensities were collected as 16-bit images using a digital chemiluminescence imaging system (c300, Azure Biosystems, Dublin, CA) at different exposure times (0.5–200 s), as described for the western blot analysis. Membranes were stripped using a mild stripping solution of 200 mM glycine, 0.1% SDS, 1% Tween-20, pH 2.2 with shaking at RT for 15 min, and re-probed with different antibodies.

Electron microscopy and axial STEM tomography

Acute hippocampal slices processed for electron microscopy analysis were prepared as described for the electrophysiology experiments, from P17 mice. Slices were microwave-fixed for 13 s in 6% glutaraldehyde, 2% PFA, 2 mM $CaCl_2$ in 0.1 N sodium cacodylate buffer and stored overnight at 4°C. After three washes in 0.1 N cacodylate buffer, we cut samples from the middle part of CA1 *s.r.*, ~100 μm away from the CA1-PC layer. These samples were treated with 1% osmium tetroxide for 1 hour on ice, en bloc mordanted with 0.25% uranyl acetate at 4°C overnight, washed and dehydrated with a graded series of ethanol, and embedded in epoxy resins. Thin sections (70–90 nm) were counterstained with lead citrate and uranyl acetate and examined on a JEOL 1200 EX transmission electron microscope. Images were collected with a CCD digital camera system (XR-100, AMT, Woburn, MA). To visualize the arrangement of pre-synaptic terminals, post-synaptic terminals, and astrocytic processes, thick sections (~1 μm) were cut from regions of CA1 *s.r.* and electron tomograms were collected in a 300 kV electron microscope operated in the scanning transmission electron microscopy (STEM) mode, as described previously (Hohmann-Marriott et al., 2009; Sousa et al., 2011). A sample thickness of 1 μm – enabled by axial STEM tomography – provided sufficient sample depth to visualize features of interest in their entirety, such as synapses. In contrast to STEM tomography, conventional TEM tomography is limited to a specimen thickness of ~400 nm and cannot be applied to such thick sections because the transmitted electrons undergo multiple inelastic scattering processes, resulting in images that are blurred by chromatic aberration of the objective lens. Axial STEM tomography is not affected by chromatic aberration because the objective lens that forms the electron probe is in front of the specimen. Dual-axis tilt series of selected sections were recorded using an FEI Tecnai TF30 TEM/STEM operating at 300 kV (1.5° tilt increment, tilt range from 55° to −55°, pixel size = 5.6 nm). Image registration, tomogram generation, tracing, surface area and volume measures were performed using IMOD 4.7 (https://bio3d.colorado.edu/imod/). In the tomograms, we identified astrocytic processes based on their lack of synaptic vesicles and post-synaptic densities and because they did not give rise to pre- or post-synaptic terminals. Orthoslices through the STEM tomograms showed that astrocytic processes contained glycogen granules, intermediate filament bundles and a more electron-lucent cytoplasm with respect to that of neurons. The astrocytic processes were traced for the entire thickness of the reconstructed volume (1–1.5 μm). We reconstructed all astrocytic processes and all PSDs in each block. The reconstructed volumes were converted into object files and imported into the open-source software Blender 2.76 (https://www.blender.org/). Astrocyte-PSD distance was measured in Blender using custom-made analysis software written in Python (Sweeney et al., 2017).

Tomographic holographic 3D microscopy

The measures of the cell membrane to cytoplasm ratio were obtained from acute hippocampal slices, prepared as described in the electrophysiology section of the methods, from animals aged P14–21 at ZT3.5 (L phase) or ZT15.5 (D phase). We used slices prepared at ZT3.5 for our osmolality test. Briefly, we prepared different batches of the slice recording solution, with different concentrations of NaCl (95, 107, 119, 131, 143 mM). We measured the osmolality of these solutions using a vapor pressure osmometer (Wescor 5600, Wescor, Logan, UT). Each slice was stored in one of these solutions for 1 hour, then it was fixed overnight with 4% PFA/PBS and cryo-protected in 30% sucrose PBS. The slices were then re-sectioned at 40 μm thickness using a vibrating blade microtome (VT1200S, Leica Microsystems, Buffalo Grove, IL) and mounted on a microscope slide using Fluoromount-G mounting medium (Cat#

0100-01; SouthernBiotech, Birmingham, AL). The slices were then imaged using the 3D Cell Explorer holographic tomographic 3D microscope (Nanolive, Ecublens, Switzerland) equipped with a 60X objective (NA = 0.8), a class I laser source at λ = 520 nm with a power output of 0.1 mW (sample exposure = 0.2 mW/mm^2), and a USB 3.0 CMOS Sony IMX174 sensor providing 1024 × 1024 pixels at 165 fps (Cotte et al., 2013). The output data were acquired as image stacks of 512 × 512 × 96 voxels (0.186 × 0.186 × 0.372 μm) with a rate of tomogram acquisition of 0.5 s^{-1}. This label-free non-phototoxic type of microscopy measures the refractive index (RI) in 3D samples, and allows users to visualize it using different levels of tolerance referred to as the refractive index gradient (IG). The acquired images were processed using Software for Tomographic Exploration of liVing cElls (STEVE) and Fiji (https://fiji.sc/). By using STEVE, we digitally stained the cells' membrane (RI = 1.327–1.333; IG = 0.015–0.070) and cytoplasm (RI = 1.329–1.330; IG = 0.007–0.021). The RI and IG settings were varied across slices, but remained constant for our measures in the CA1-PC layer and *s.r.* of hippocampal area CA1. By using Fiji, we calculated the number of digitally stained pixels in three ROIs (200 × 100 × 40 pixels) positioned in the CA1-PC layer and *s.r.* of each slice. The center of the ROIs along the z axis was positioned half way through the original z stack acquired using the 3D Cell Explorer.

NEURON modeling

3D z stacks of biocytin filled CA1-PCs were acquired using a Zeiss LSM710 confocal microscope and saved as czi files. The czi files were processed with 4x4 binning and imported into Fiji (https://fiji.sc/) using the Simple Neurite tracer v3.1.3 plugin (https://imagej.net/Simple_Neurite_Tracer), first developed by (Longair et al., 2011). The radius of the soma was calculated as the radius of an equivalent circle with the same area of the soma obtained from the maximum intensity projection of the confocal z stacks. When using this plugin, we first picked the location of the center of the soma and then manually traced the 3D trajectory of different neuronal processes. Each process was tagged as axon, basal or dendritic branch so that they could be assigned different conductances. The tracings were converted into .swc and .asc files to be imported in the NEURON simulation environment v7.6 (Hines and Carnevale, 1997). All model and simulation files are uploaded to the ModelDB database (https://senselab.med.yale.edu/modeldb/, acc.n. 257027). The morphology is uploaded to the neuromorpho.org database (https://www.neuromorpho.org), and an interactive "live paper" page is setup in the Brain Simulation Platform of the Human Brain Project (https://humanbrainproject.github.io/hbp-bsp-live-papers/2020/mccauley_et_al_2020/mccauley_et_al_2020.html). To implement a CA1-PC model, we used the 3D accurate morphology reconstructed within this work (Figure 5D) equipped with the typical somatodendritic distribution of channels observed in rodents hippocampal CA1-PCs (Migliore and Shepherd, 2002). The channel kinetics were identical to those used in (Migliore et al., 2018) (ModelDB acc.n. 244688). The AMPA synapse kinetic model was from (Tsodyks et al., 1998) (ModelDB acc.n. 3815), with *tau_1* = 4.5 ms, a peak conductance of 0.2 nS, and a *tau_rec* of 10 ms or 30 ms to model light and dark condition, respectively. The NMDA kinetics was taken from (Gasparini et al., 2004) (ModelDB acc.n. 44050) with the reverse (unbinding) rate β = 0.005 ms^{-1} and a peak conductance of 0.7 nS or 0.55 nS to reproduce L and D phase conditions, respectively. To mimic the train of synaptic activations caused by extracellular electrical pulses, we added 20 synapses randomly distributed in the apical dendrites between 50 and 300 μm from the soma, synchronously activated every 10-100 ms.

CellBlender modeling

We performed 3D Monte Carlo reaction-diffusion simulations using the CellBlender bundle for Blender 2.79 (Windows 10), which includes Blender 2.79 and the CellBlender 1.1 add-on (https://mcell.org/). We built an *in silico* representation of the synaptic environment including an axon with a bouton (green), a spine with its parent dendritic branch (*gold*) and four neighboring astrocytic processes (*blue*; Figure 5L). The axon had a radius r = 125 nm and contained a spherical bouton with r = 250 nm. The bouton was positioned 20 nm away from the spine, a distance that matches the typical height of the synaptic cleft. The spine radius was also r = 250 nm. The spine head was connected to the dendritic shaft by a thin (r = 50 nm), 500 nm long neck. The dendritic shaft was 2 μm long, with r = 500 nm. The bouton-spine interface was flanked by four astrocytic processes with radius r = 100 nm (Sweeney et al., 2017). Each astrocyte process expressed glutamate transporters with surface density d = 10,800 μm^2 (Lehre and Danbolt, 1998). Each transporter was modeled using a simplified 3-state kinetic scheme included in Figure S6. based on kinetic models for glutamate transporters developed by (Barbour, 2001) and (Bergles et al., 2002), also used in our own previous work (Sweeney et al., 2017). In this scheme, the glutamate binding, translocation and re-orientation rates were consistent with estimates from the model of (Bergles et al., 2002). The glutamate-unbinding rate was derived from the equation of the apparent steady state affinity for glutamate, with k_m = 13 μM (Barbour, 2001):

$$k_m = \frac{k_2 k_4 + k_3 k_4}{k_1 \cdot (k_3 + k_4)} \quad \text{(Eq. 1)}$$

All kinetic rates were adjusted for Q_{10} = 3, to approximate the receptor and transporter kinetics at physiological temperature (36°C). At the beginning of each simulation, we released 2,000 glutamate molecules from a point source placed in the center of the synaptic cleft. The apparent glutamate diffusion coefficient in the synaptic cleft was D^*_{in} = 3.3 e-6 cm^2/s (Nielsen et al., 2004). The hindrance to diffusion within the cleft is mainly due to the interstitial viscosity, estimated as λ_v = 1.2 (Nicholson and Hrabětová, 2017). Therefore

$\lambda_{in} = \lambda_v = 1.2$. The extracellular tortuosity is typically $\lambda_{out} = 1.6$. Because the apparent diffusion coefficient D* is inversely proportionate to λ^2, it follows that:

$$\frac{D^*_{out}}{D^*_{in}} = \frac{\lambda^2_{in}}{\lambda^2_{out}} = \frac{1.2^2}{1.6^2} = 0.56 \quad \text{(Eq. 2)}$$

Since $D^*_{in} = 3.3$ e-6 cm^2/s, this means that $D^*_{out} = 1.85$e-6 cm^2/s. The apparent diffusion coefficient for glutamate changed from D^*_{in} to D^*_{out} as glutamate diffused away from a 250 nm radius cleft centered at the top of the spine head. Each simulation was run within a 1.6 μm·2.2 μm·2.6 μm world with absorptive properties for glutamate. The results were averaged across 100 seeds (i.e., 100 simulations) using custom made code written in Python 3 (A. Scimemi).

Data analysis

Electrophysiological recordings were analyzed within the Igor Pro environment using custom made software (A. Scimemi). Synaptically activated transporter currents (STCs) were isolated as described previously (Diamond, 2005; Scimemi et al., 2009; Sweeney et al., 2017). Briefly, single and pairs of stimuli, 100 ms apart, were delivered every 10 s. We averaged 10 single and 10 STC pairs and subtracted single from paired STCs to isolate the current evoked by the second pulse. The single STC was then shifted in time by 100 ms (the inter-pulse interval), so that its onset matched the onset of the second STC. The current obtained by subtracting the time-shifted single STC from the paired STCs represented the facilitated portion of the STC (fSTC). This analytical strategy allowed us to get rid of the sustained potassium current that is superimposed on the STC but does not facilitate with repeated stimulation. In the unlikely event that a component of the sustained potassium current was still present after this subtraction, we removed it by subtracting a mono-exponential function with an onset time of 4 ms and an amplitude that was scaled to match the amplitude of the remaining potassium current (Scimemi et al., 2009). We used the fSTCs in control conditions and in the presence of a sub-saturating concentration of TFB-TBOA (1 μM) to calculate the time course of glutamate clearance by performing a deconvolution analysis of the STCs (Diamond, 2005; Scimemi et al., 2009; Sweeney et al., 2017). *First,* the STCs recorded under control conditions and in TFB-TBOA (1 μM) were binomially smoothed and fitted with the following equation (Nielsen et al., 2004):

$$F(t) = A_1\left(1 - e^{\frac{t_0 - t}{\tau_{rise}}}\right)^n \left(e^{\frac{t_0 - t}{\tau_{fast}}} + A_2 e^{\frac{t_0 - t}{\tau_{slow}}}\right) \quad \text{(Eq. 3)}$$

Second, we approximated glutamate clearance in TFB-TBOA (1 μM) with an instantaneously rising function decaying mono-exponentially, with the same time course of the STC. *Third,* we deconvolved this approximated glutamate clearance from the STC recorded in low TFB-TBOA to obtain the filter. *Fourth,* we deconvolved the filter from the STC recorded in control conditions to obtain the glutamate clearance waveform in control conditions.

Miniature events were detected using an optimally scaled template (Clements and Bekkers, 1997) adapted for Igor Pro (A. Scimemi). The EPSC PPR was calculated by subtracting single from paired EPSCs averaged across 20 traces, after first peak normalization. When delivering trains of stimuli, we interleaved single pulses with trains of four and five pulses. The 5th EPSC was isolated by subtracting the average response to four pulses from the average response to five pulses.

Image preprocessing for Sholl analysis

The Sholl analysis was performed on adaptively thresholded maximum intensity projections of filtered confocal z stacks. Each plane of the z stack was first filtered with a coherence-enhancing diffusion filter (Weickert and Scharr, 2002), and then we filtered the maximal projection intensity image as described below. Astrocytic processes are generally thin and elongated. To take advantage of this property, we used steerable oriented filters and stored in each pixel the maximal response to different filter sets. Any region near a round bright spot is ''oriented'' toward it, meaning that the maximal response is obtained with respect to the filter with similar orientation. We used a round isotropic Gaussian filter to find local intensity maxima and oriented filters to highlight the thin elongated structures. To suppress the algorithm from detecting false-positive filamentous structures in dark and noisy regions of interest we performed a randomization-based regularization consisting of many iterations in which we disturbed the input image with noise and then thresholded the responses. By averaging the results obtained over multiple iterations, we obtained an estimate of the probability that each pixel has an oriented structure brighter than its surroundings. The final mask is the product of the isotropic and anisotropic filter responses.

Image analysis of complexity and entropy

The complexity-entropy analysis allows quantification of the spatial properties of representative images with respect to their balance between randomness and structural order, triviality and complexity as previously described (Brazhe, 2018). In mathematical terms, this is described as location in the complexity-entropy plane or their distribution along a complexity-entropy spectrum. Highly ordered structures (e.g., a regular grating) have near-zero entropy and near-zero complexity. In contrast, completely disordered structures (e.g., independent and identically distributed Gaussian samples) have maximal entropy and small statistical complexity. Intermediate values of entropy are associated with higher values of complexity if the underlying pattern contains features with preferred orientation. For example, signals generated by systems with deterministic chaos result in a complexity-entropy spectrum with near-0.5 peak complexity and near-0.7 entropy (Lamberti et al., 2004; Rosso et al., 2007). The implementation code is available at https://

doi.org/10.5281/zenodo.1217636. Briefly, complexity and entropy measures can be based on a feature distribution of the analyzed patterns, which can be compared to equally probable or singular feature cases. Accordingly, the relative entropy (H) was defined as the Shannon entropy:

$$H[P] : \frac{S[P]}{S_{max}} = \left(-\sum_{i=1}^{N} P_i \log_2 P_i \right) \Big/ \log_2 N \quad \text{(Eq. 4)}$$

normalized by the entropy of an equally probable distribution (S_{max}), thus giving values in the range [0 … 1]. Here N is the number of features analyzed. The complexity measures were based on the notion of disequilibrium (Lamberti et al., 2004) and defined in terms of normalized Jensen-Shannon divergence from an equally probable distribution (Rosso et al., 2007):

$$C[P] : H[P]J[P, P_e]/J_{max} \quad \text{(Eq. 5)}$$

In this expression, $J[P,P_e]$ is Jensen-Shannon divergence of some distribution P from an equally probable distribution P_e:

$$J[P, P_e] = S\left[\frac{P + P_e}{2}\right] - \frac{1}{2}(S[P] + S[P_e]) \quad \text{(Eq. 6)}$$

and J_{max} is obtained when the probability of just one feature is equal to 1, while the probability of all other features is zero. The defined probability-based definitions of entropy and complexity require building descriptive probability-like measures for spatial patterns, preferably allowing for multiscale resolution and local analysis. A spatial pattern can be described in terms of local edge orientations and scales, which can be achieved by discrete shearlet transform, which is analogous to wavelet transform with added orientation information. We treated normalized power of shearlet coefficients as probability densities of given spatial feature orientation and scale at a given location. Complexity and entropy calculations were only performed in regions containing non-zero pixels, while other areas were masked out.

Novel object recognition test

We performed novel object recognition test on C57BL/6NCrl mice of either sex, maintained on as 12 h:12 h L/D or D/D cycle. The mice were aged P16 on the first training session and P22 on the testing session. The task was conducted either at ZT3.5 or ZT15.5 in a white Plexiglas box (L: 46 cm × W: 46 cm × H: 38 cm). Each mouse was video monitored for 10 min at 30 fps using a Night Vision CMOS IR USB 2.0 webcam (Model #B07PNHJP8J from webcamera_usb). We analyzed the position of the mouse in four adjacent quadrants of the arena (top left, top right, bottom left, bottom right) using ezTrack (Pennington et al., 2019). The test including one habituation session, five training sessions and one testing session. Briefly, during the first habituation session, we positioned a mouse in the open field arena and allowed it to freely explore it for 10 min. During each training session, we re-introduced the mouse in the open field arena, after positioning a non-familiar object in its top right corner. The novel object was a metal parallelepiped. During the test session, we removed the object from the arena and allowed the mouse to explore the open field. We calculated the proportion of time spent in the top right corner of the arena during each of the seven sessions using ezTrack. The learning discrimination index was calculated as the difference in the proportion of time spent in the top right corner between the second and first session. The memory discrimination index was calculated as the difference in the proportion of time spent in the top right corner of the arena between the seventh and sixth session.

QUANTIFICATION AND STATISTICAL ANALYSIS

Data are presented as mean ± SEM unless otherwise stated. All experiments were performed on multiple mice of either sex. Statistical significance was determined by Student's paired or unpaired t test or ANOVA, as appropriate (IgorPro 6.37). Differences were considered significant at $p < 0.05$ (*$p < 0.05$; **$p < 0.01$; ***$p < 0.001$).

Cell Reports, Volume *33*

Supplemental Information

Circadian Modulation of Neurons and Astrocytes Controls Synaptic Plasticity in Hippocampal Area CA1

John P. McCauley, Maurice A. Petroccione, Lianna Y. D'Brant, Gabrielle C. Todd, Nurat Affinnih, Justin J. Wisnoski, Shergil Zahid, Swasti Shree, Alioscka A. Sousa, Rose M. De Guzman, Rosanna Migliore, Alexey Brazhe, Richard D. Leapman, Alexander Khmaladze, Alexey Semyanov, Damian G. Zuloaga, Michele Migliore, and Annalisa Scimemi

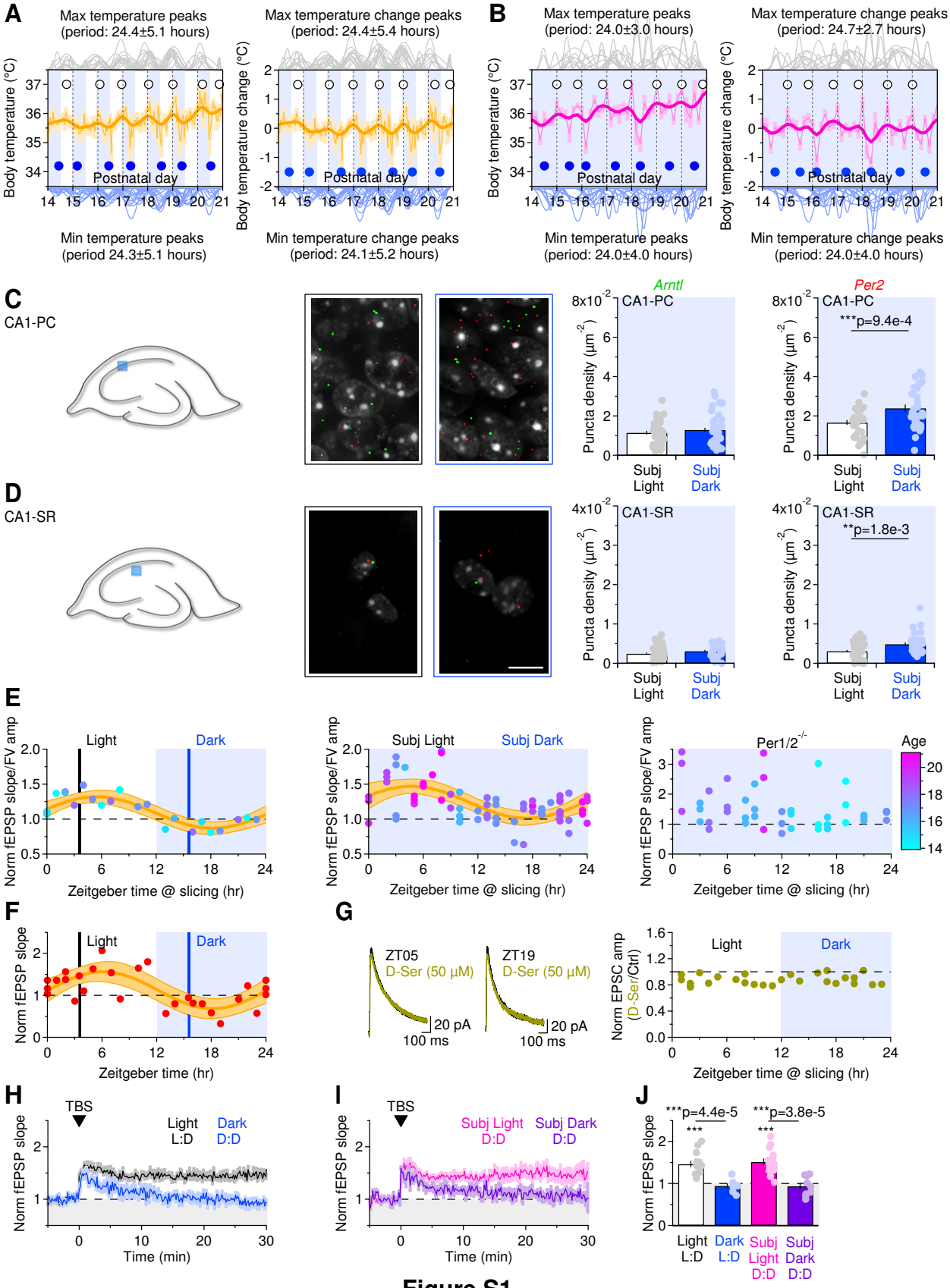
A
Max temperature peaks
(period: 24.4±5.1 hours)
Max temperature change peaks
(period: 24.4±5.4 hours)
Body temperature (°C)
Body temperature change (°C)
Postnatal day
Min temperature peaks
(period 24.3±5.1 hours)
Min temperature change peaks
(period: 24.1±5.2 hours)
B
Max temperature peaks
(period: 24.0±3.0 hours)
Max temperature change peaks
(period: 24.7±2.7 hours)
Min temperature peaks
(period: 24.0±4.0 hours)
Min temperature change peaks
(period: 24.0±4.0 hours)
C
CA1-PC
Arntl
Per2
Puncta density (µm-2)
***p=9.4e-4
Subj Light
Subj Dark
D
CA1-SR
**p=1.8e-3
E
Light
Dark
Norm fEPSP slope/FV amp
Zeitgeber time @ slicing (hr)
Subj Light
Subj Dark
Per1/2-/-
Age
F
Norm fEPSP slope
Zeitgeber time (hr)
G
ZT05
D-Ser (50 µM)
ZT19
D-Ser (50 µM)
20 pA
100 ms
Norm EPSC amp
(D-Ser/Ctrl)
H
TBS
Light L:D
Dark D:D
Time (min)
I
Subj Light D:D
Subj Dark D:D
J
***p=4.4e-5
***p=3.8e-5
Light L:D
Dark L:D
Subj Light D:D
Subj Dark D:D

Figure S1

Figure S1 (Related to Fig. 1). Circadian oscillations in body temperature, hippocampal clock gene expression and synaptic plasticity in juvenile mice. (A) *Left,* Body temperature values measured using subcutaneous transponders on P14-21 mice (n=14). *Right*, As in *left*, after subtraction of the mean body temperature of each mouse averaged over the entire duration of the experiment. White and blue shaded areas: hours of light exposure (ZT0-12) and darkness (ZT12-24), respectively. White and blue dots: position of the maximum and minimum temperature peaks, respectively. Thin orange line and yellow shaded areas: mean ± SEM. Thick orange line: smoothed mean, obtained using a boxcar smoothing algorithm with 10 repetitions and a 5-point boxcar width. Grey and blue curves: multi-peak fit of the data collected from each mouse, to determine the position of the maximum (*top*) and minimum body temperature for each mouse (*bottom*). **(B)** As in (A), for mice kept in 12H:12H D:D conditions (n=13). **(C)** Schematic representation of a mid-sagittal section of the mouse brain, with light blue square showing the location of the region from which we collected confocal images. The fluorescence micrograph shows the results of RNAscope *in situ* hybridization for transcripts of clock genes *Arntl* (*green*) and *Per2* (*red*), at ZT3.5 (SL) and ZT15.5 (SD) in mice kept under constant darkness. The bar charts provide a summary of the *Arntl* and *Per2* puncta density (SL: n=35, SD: n=32). Data: mean ± SEM. Scale bar: 10 μm. **(D)** As in (C), for *s.r. Arntl* (SL: n=38, SD: n=33) and *Per2* (SL: n=47, SD: n=33). Data: mean ± SEM. **(E)** As in **Fig. 1D**, with the color of each dot representing the mouse age. **(F)** Analysis of TBS-induced changes in fEPSP slope, for the experiments described in **Fig. 1D**, *left*. **(G)** *Left,* Averages of 20 consecutive NMDA EPSCs acquired under baseline conditions (*black*) or in the presence of D-Serine (50 μM), at ZT5 and ZT19. *Right,* Effect of D-Serine on the NMDA EPSC amplitude. **(H)** Analysis of TBS-induced changes in fEPSP slope, for the experiments described in **Fig. 1E**, *top left*. **(I)** Analysis of TBS-induced changes in fEPSP slope, for the experiments described in **Fig. 1E**, *bottom left*. **(J)** Effect of TBS on the fEPSP slope (L: n=13, D: n=7, SL: n=14, SD: n=9). Data: mean ± SEM.

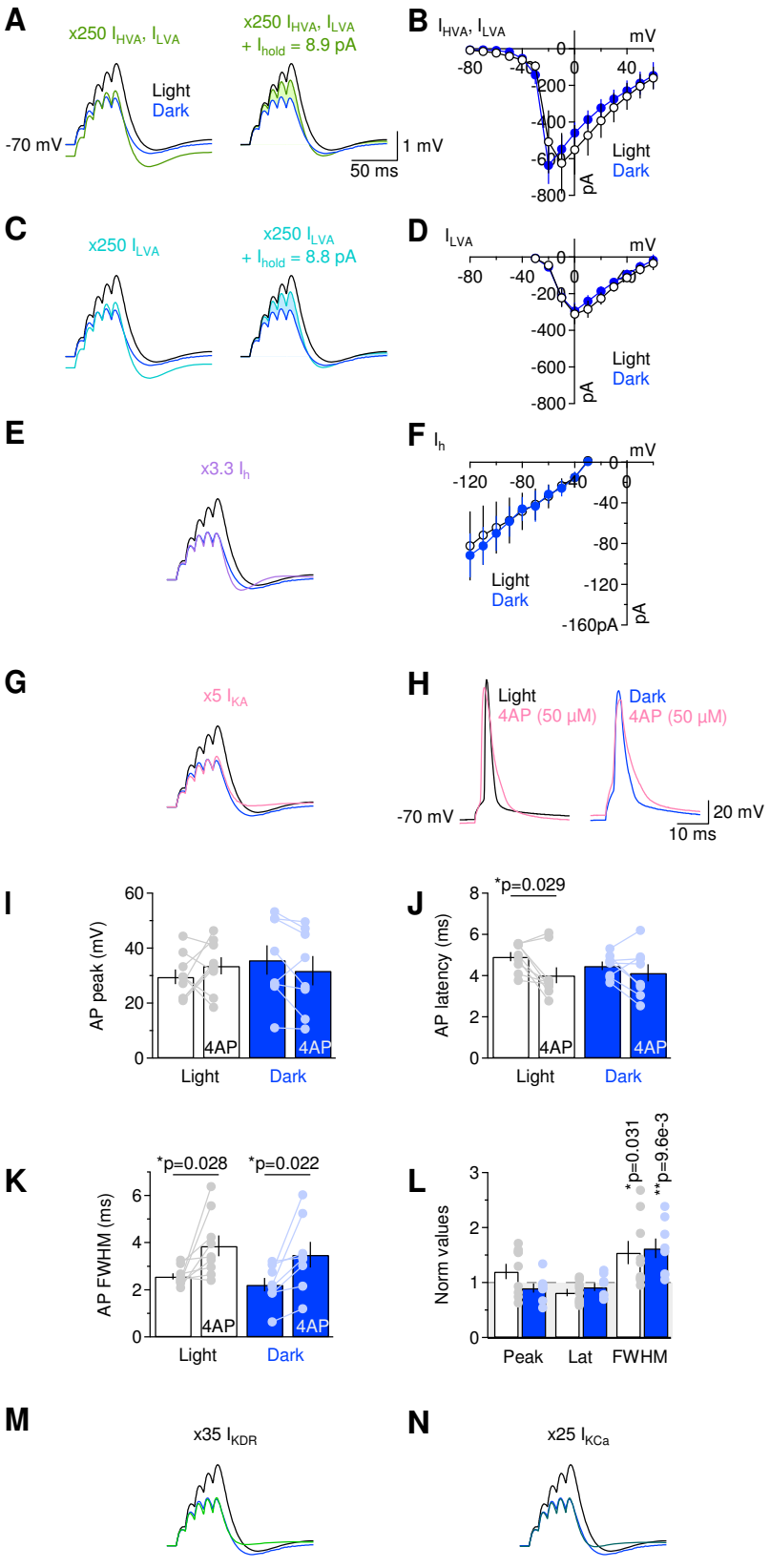
A
x250 I_HVA, I_LVA
x250 I_HVA, I_LVA
+ I_hold = 8.9 pA
Light
Dark
-70 mV
1 mV
50 ms
B
I_HVA, I_LVA
mV
pA
Light
Dark
C
x250 I_LVA
x250 I_LVA
+ I_hold = 8.8 pA
D
I_LVA
E
x3.3 I_h
F
I_h
G
x5 I_KA
H
Light
4AP (50 µM)
Dark
4AP (50 µM)
-70 mV
20 mV
10 ms
I
AP peak (mV)
4AP
Light
Dark
J
*p=0.029
AP latency (ms)
K
*p=0.028
*p=0.022
AP FWHM (ms)
L
*p=0.031
**p=9.6e-3
Norm values
Peak
Lat
FWHM
M
x35 I_KDR
N
x25 I_KCa

Figure S2

Figure S2 (Related to Fig. 2). Comparison of modeling and experimental data on the contribution of different ionic conductances to the reduced temporal summation of excitatory inputs in the D-phase. **(A)** Results of NEURON multi-compartmental model evoked by activating 100 synapses randomly distributed through CA1-PC dendrites. The trace in green was obtained by imposing a 250-fold increase in the conductance of HVA and LVA calcium channels in the model. The traces on the right were obtained by injecting 8.9 pA positive holding current, to ensure the resting membrane potential was similar to that of L/D-phase simulations. **(B)** I/V plot obtained by recording HVA and LVA currents from CA1-PCs, evoked by 100 ms voltage step depolarization of increasing amplitude (L: n=6, D: n=5). Data: mean ± SEM. **(C)** As in (A), in response to a 250-fold increase in the conductance of LVA calcium channels (*left*) and after injection of 8.8 pA holding current (*right*). **(D)** I/V plot obtained by recording LVA currents from CA1-PCs, evoked by 100 ms voltage step depolarization of increasing amplitude (L: n=6, D: n=5). Data: mean ± SEM. **(E)** As in (A, *left*), in response to a 3.3-fold increase in the conductance of I_h channels. **(F)** I/V plot obtained by recording I_h currents from CA1-PCs, evoked by 100 ms voltage step depolarization of increasing amplitude (L: n=7, D: n=5). Data: mean ± SEM. **(G)** As in (A, *left*), in response to a 5-fold increase in the conductance of I_A potassium channels. **(H)** Example of action potentials recorded in control conditions, in the L/D-phases, and following application of the I_A antagonist 4AP (50 µM). The action potentials were evoked by applying a 5-ms long, supra-threshold current step injection to CA1-PCs. **(I)** Summary and in-cell comparison of the effect of 4AP on the action potential peak (L: n=9, D: n=8). Data: mean ± SEM. **(J)** As in (I), for action potential latency (L: n=9, D: n=8). Data: mean ± SEM. **(K)** As in (I), for action potential FWHM (L: n=9, D: n=8). Data: mean ± SEM. **(L)** Baseline-normalized action potential peak, latency and FWHM in the presence of 4AP (L: n=9, D: n=8). Data: mean ± SEM. **(M)** As in (A, *left*), in response to a 35-fold increase in the conductance of I_{DR} potassium channels. **(N)** As in (A, *left*), in response to a 25-fold increase in the conductance of I_{KCa}.

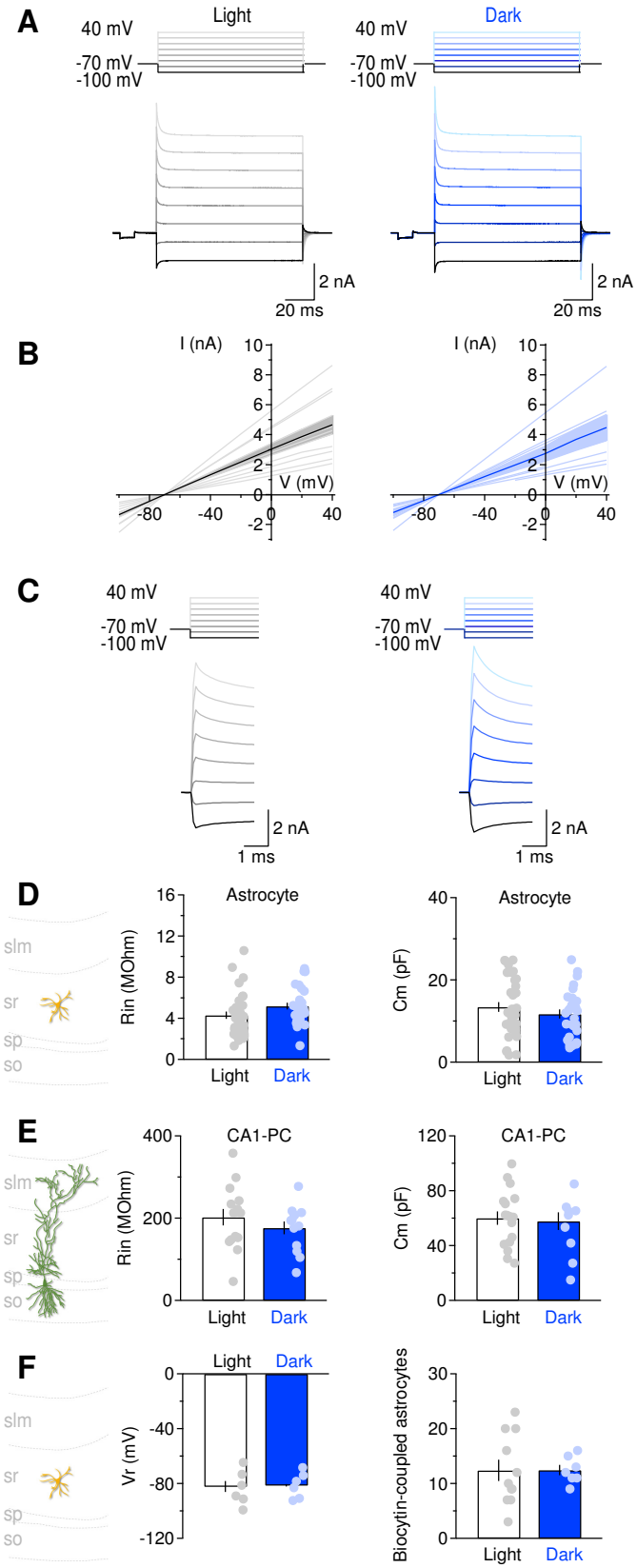
A
Light
Dark
40 mV
-70 mV
-100 mV
2 nA
20 ms
B
I (nA)
V (mV)
C
1 ms
D
Astrocyte
Rin (MOhm)
Cm (pF)
Light
Dark
slm
sr
sp
so
E
CA1-PC
F
Vr (mV)
Biocytin-coupled astrocytes

Figure S3

Figure S3 (Related to Fig. 4). The passive membrane properties of astrocytes and neurons do not change during the L/D-phases. (A) Example of voltage step protocol and current responses recorded from astrocytes patched in *s.r.* of acute hippocampal slices in the L/D-phases. Each current response represents the average of 20 responses from one astrocyte. **(B)** I/V relationship derived from the experiment described in (A) (L: n=11, D: n=8). Thick lines and shaded areas: mean ± SEM. **(C)** Close-up view on the voltage step protocol and current responses. **(D)** Astrocyte input resistance (*left*) and membrane capacitance (*right*) (L: n=35, D: n=28). Data: mean ± SEM. **(E)** As in (D), for CA1-PCs (L: n=15, D: n=13). Data: mean ± SEM. **(F)** Astrocyte resting membrane potential (L: n=9, D: n=6) and biocytin coupling (L: n=11, D: n=7). Data: mean ± SEM.

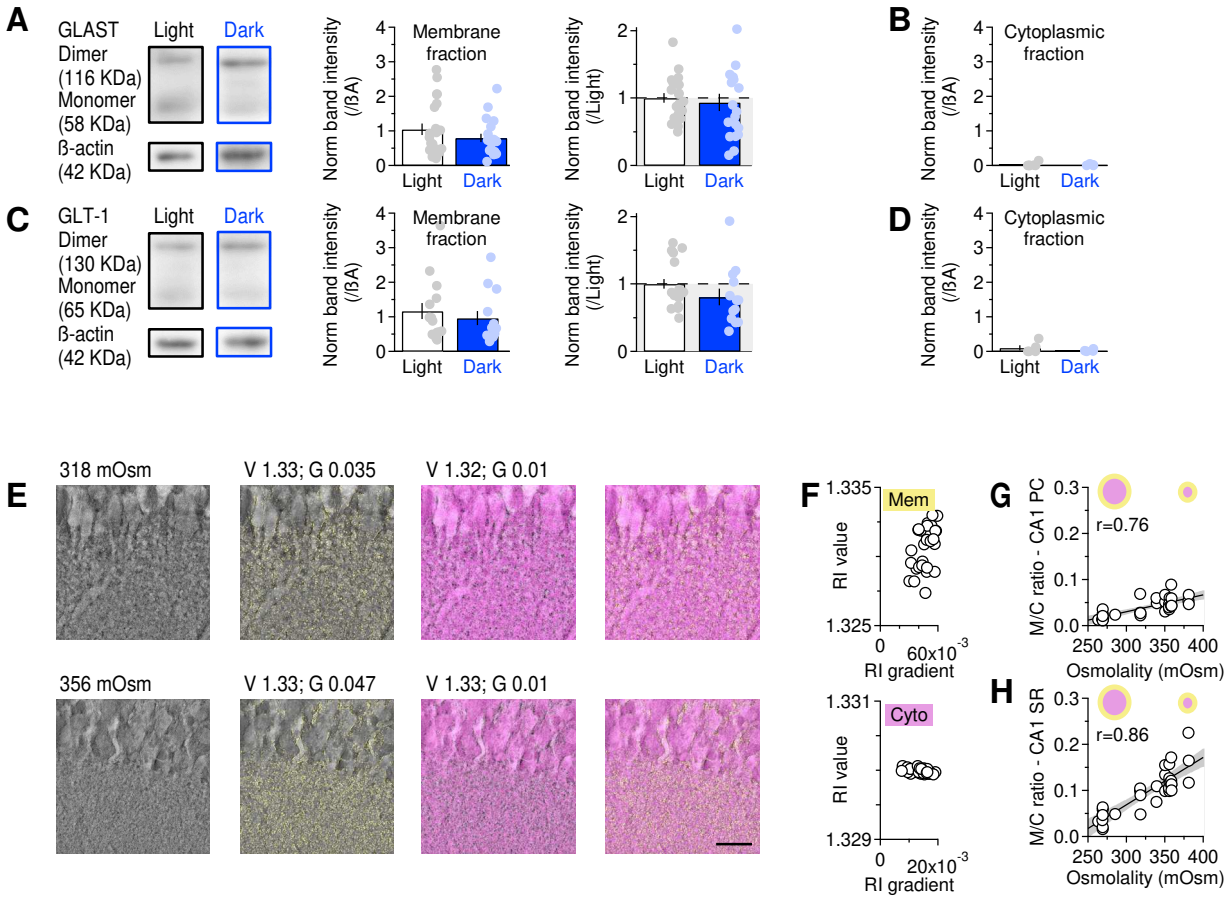
A
GLAST
Dimer
(116 KDa)
Monomer
(58 KDa)
ß-actin
(42 KDa)
Light
Dark
Norm band intensity (/βA)
Membrane fraction
Norm band intensity (/Light)
B
Cytoplasmic fraction
C
GLT-1
Dimer
(130 KDa)
Monomer
(65 KDa)
ß-actin
(42 KDa)
D
E
318 mOsm
V 1.33; G 0.035
V 1.32; G 0.01
356 mOsm
V 1.33; G 0.047
V 1.33; G 0.01
F
Mem
Cyto
RI value
RI gradient
60x10-3
20x10-3
G
M/C ratio - CA1 PC
r=0.76
Osmolality (mOsm)
H
M/C ratio - CA1 SR
r=0.86

Figure S4

Figure S4 (Related to Fig. 5). Detection of GLAST and GLT1 membrane expression and validation of holotomography approach to measure cell shrinkage and swelling. (A) *Left,* Western blot analysis of biotinylated hippocampal GLAST expression. *Middle,* GLAST band intensity in the membrane fraction, normalized to the corresponding intensity of β-actin. *Right*, As in *middle*, after further normalization by the band intensity in the L-phase (L: n=21, D: n=19). Data: mean ± SEM. **(B)** Quantification of GLAST band intensity in the cytoplasmic fraction, divided by the β-actin normalized band intensity in the L-phase (L: n=7, D: n=7). Data: mean ± SEM. **(C)** As in (A), for GLT1 (L: n=15, D: n=13). Data: mean ± SEM. **(D)** As in (B), for GLT1 (L: n=5, D: n=5). Data: mean ± SEM. **(E)** Example images of hippocampal area CA1, collected using holotomography in slices stored in extracellular solutions of different osmolality. Each image was digitally stained using refractive index (RI) value (V) and gradient (G) combinations that allowed labeling cell membranes (*yellow*) and cell cytoplasm (*magenta*). Scale bar: 20 μm. **(F)** Scatter plot of RI value and gradient combinations used to label cell membranes (*left, yellow*) and cytoplasm (*right, magenta*: n=32). **(G)** M/C ratio measures in the CA1-PC layer (n=32). **(H)** As in (G), for measures collected from *s.r.* (n=32).

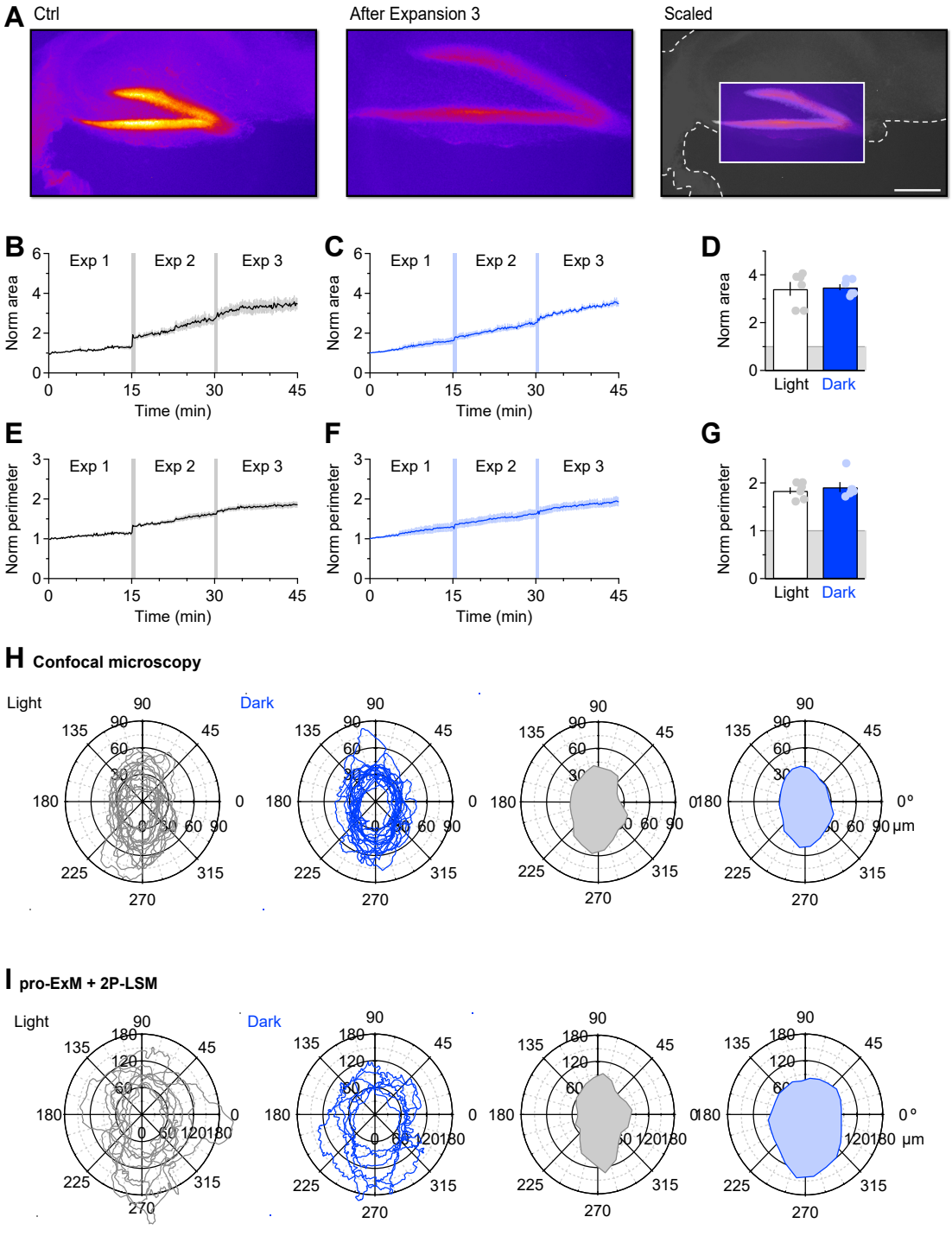
A
Ctrl
After Expansion 3
Scaled
B
Exp 1
Exp 2
Exp 3
Norm area
Time (min)
C
D
Light
Dark
E
Norm perimeter
F
G
H Confocal microscopy
Light
Dark
I pro-ExM + 2P-LSM
μm

Figure S5

Figure S5 (Related to Fig. 5). proExM provides a similar expansion of hippocampal slices prepared during the L/D-phases. (A) *Left,* fluorescence micrograph of a hippocampal slice labelled with DAPI. The high cell density, bright area is the dentate gyrus. *Middle,* fluorescence micrograph of the same hippocampal slice after three consecutive, 15 min long rounds of expansion. *Right,* overlaid image of the expanded dentate gyrus scaled down to the size of the hippocampal slice before expansion. Scale bar: 1 mm. **(B)** Time course of hippocampal slice area increase during the proExM protocol, in the L-phase (n=6). Data: mean ± SEM. **(C)** As in (B), in the D-phase (n=6). Data: mean ± SEM. **(D)** Quantification of the proExM-induced surface area increase in hippocampal slices (L: n=6, D: n=6). Data: mean ± SEM. **(E)** Time course of hippocampal slice perimeter increase during the proExM protocol, in the L-phase (n=6). Data: mean ± SEM. **(F)** As in (E), in the D-phase (n=6). Data: mean ± SEM. **(G)** Quantification of the proExM-induced perimeter increase in hippocampal slices (L: n=6, D: n=6). Data: mean ± SEM. **(H)** Polar plots of astrocyte contours after confocal imaging (*top*) and their corresponding averages (*right*; L: n=15, D: n=17). **(I)** Polar plots of astrocyte contours after proExM and 2P-LSM (*top*) with their corresponding averages (*right*; L: n=9, D: n=6).

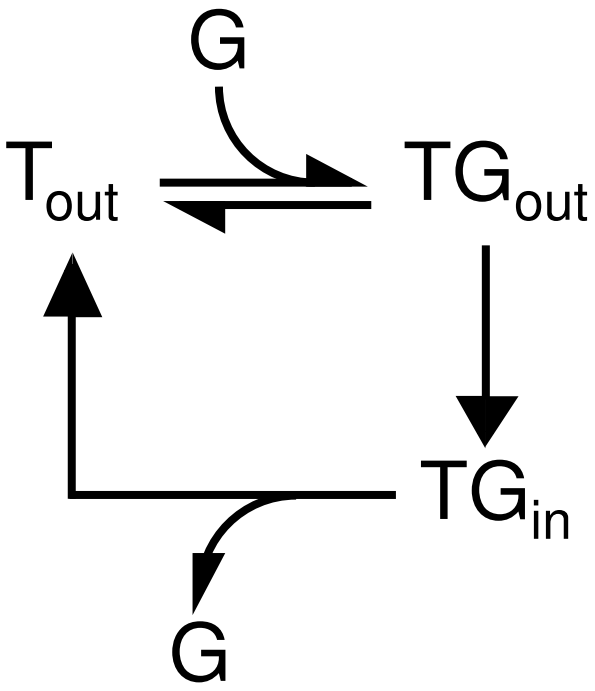

T_{out} +G	$\rightarrow TG_{out}$	k_1 = 6e6 M^{-1} s^{-1}
TG_{out}	$\rightarrow TG_{out}$ + G	k_2 = 1198 s^{-1}
TG_{out}	$\rightarrow TG_{in}$	k_3 = 2e3 s^{-1}
TG_{in}	$\rightarrow T_{out}$ + G	k_4 = 50 s^{-1}

Figure S6

Figure S6 (Related to Fig. 5). Kinetic scheme of glutamate transporters. Simplified 3-state kinetic scheme, based on existing kinetic models for glutamate transporters (Barbour, 2001; Bergles et al., 2002). The glutamate binding, translocation and re-orientation rates are consistent with estimates from (Bergles et al., 2002), and the glutamate-unbinding rate is derived from the equation of the apparent steady state affinity for glutamate, with k_m=13 µM (Barbour, 2001). All kinetic rates are adjusted for Q_{10}=3, to approximate the receptor and transporter kinetics at physiological temperature (36°C).